J. Fluid Mech. (1998), *vol.* 359, *pp.* 49–79. Printed in the United Kingdom

Characteristics of endwall and sidewall boundary layers in a rotating cylinder with a differentially rotating endwall

By J. M. LOPEZ

Department of Mathematics and Earth System Science Center, The Pennsylvania State University, University Park, PA 16802, USA

(Received 27 May 1997 and in revised form 3 November 1997)

The flow in a rotating cylinder driven by the differential rotation of its top endwall is studied by numerically solving the time-dependent axisymmetric Navier–Stokes equations. When the differential rotation is small, the flow is well described in terms of similarity solutions of individual rotating disks of infinite radius. For larger differential rotations, whether the top is co-rotating or counter-rotating results in qualitatively distinct behaviour. For counter-rotation, the boundary layer on the top endwall separates, forming a free shear layer and this results in a global coupling between the boundary layer flows on the various walls and a global departure from the similarity flows. At large Reynolds numbers, this shear layer becomes unstable. For a co-rotating top, there is a qualitative change in the flow depending on whether the top rotates faster or slower than the rest of the cylinder. When the top rotates faster, so does the bulk of the interior fluid, and the sidewall boundary layer region where the fluid adjusts to the slower rotation rate of the cylinder is centrifugally unstable. The secondary induced meridional flow is also potentially unstable in this region. This is manifested by the inflectional radial profiles of the vertical velocity and azimuthal vorticity in this region. At large Reynolds numbers, the instability of the sidewall layer results in roll waves propagating downwards.

1. Introduction

The study of flows driven between rotating disks has been and continues to be an area of intense research for several reasons. On the one hand, these flows are of fundamental interest as in certain limits they admit exact solutions to the Navier–Stokes equations. Confined rotating flows have also attracted much attention as a test-bed for contemporary ideas on the role played by low-dimensional dynamical systems theory on the transition to spatio-temporal complexity and turbulence (e.g. Gullob & Swinney 1975; Mullin 1993). These flows are also of practical importance in many areas, such as rotating machinery and in models of wind-driven ocean circulations. A good deal of the work has focused on the case of disks of infinite radius. In the semi-infinite region bound by a single rotating disk, von Kármán (1921) gives a solution to the Navier–Stokes equations which depends only on the scaled distance normal to the disk. Bödewadt (1940) considered the case of flow above a stationary disk with the outer flow in solid-body rotation, also finding that this flow can be described by a steady similarity solution of the Navier–Stokes equations. Batchelor (1951) generalized these solutions to describe the steady flows between two coaxial rotating disks of infinite radius. He does not explicitly solve the governing

equations, but using physical arguments and properties of the ordinary differential equations that result from the similarity formulation, predicts the nature of the flow. Stewartson (1953) also considered these flows and, particularly when the disks are counter-rotating, drew different conclusions to Batchelor regarding the nature of the flow. Subsequently, there have been many attempts to resolve these differences. However, it would appear that the differences are not to be resolved in the context of infinite disks due to the ambiguity of what happens to the flow at large radius: the fluid that is centrifuged out by the disk boundary layers must be replaced by the fluid in the interior between the layers, thereby establishing a secondary circulation. However, the circuit is not complete in the infinite disk scenario.

Brady & Durlofsky (1987) presented results from an asymptotic-numerical investigation of the flow between two finite counter-rotating disks. They considered flows with Reynolds numbers, based on the distance between the disks, up to 500 and disk rotation ratios between 0 and -1. Their approach asymptotically matches the interior flow between disks of large radii, compared to the distance between them, in a boundary-layer-like formulation to that in the end region of the disks and to that near the axis. They employed two matching conditions: 'open' to simulate unshrouded disks and 'closed' to simulate shrouded disks. However, their 'closed' condition is inviscid and does not distinguish between a stationary and a rotating cylindrical shroud. To a first approximation, they note that whether the shroud rotates or not makes no difference since it is inviscid, and quote experimental observations of Dijkstra & van Heijst (1983) that tend to support this. The results from the Brady & Durlofsky (1987) study show that the effects of the end conditions are not confined to a region near the end of the disks, and that the type of end condition used (open or closed) is important in determining the form of the flow throughout the whole domain.

The experiments and numerical simulations of Dijkstra & van Heijst (1983) for the flow between two counter-rotating disks enclosed by a cylinder revealed a dramatic global departure from self-similar flow, this being due to the separation of the endwall boundary layer on the slower disk to form a shear layer in the interior of the flow.

More recent interest in this class of problems comes from laboratory models used to study the structure of vertical boundary layers in differentially rotating systems and other processes in geophysical systems. Hart & Kittelman (1996) consider the flow in a rotating cylinder that is driven by the differential rotation of the top endwall. They observe a number of waves that appear in the sidewall boundary layer region and present tentative physical arguments to explain the origin of these instabilities. However, there is a lack of knowledge concerning the basic state of this differentially rotating system from which to study its stability. The flow is related to the closed system considered earlier by Brady & Durlofsky (1987) and Dijkstra & van Heijst (1983). However, those studies only presented results for counter-rotation whereas the instabilities reported by Hart & Kittelman (1996) were observed for co-rotation.

In the present study, we present a systematic description of the flow in a cylinder of radius R and height H with the bottom and sidewall in basic rotation Ω, filled with fluid of kinematic viscosity ν, that is driven by its top lid rotating at $s\Omega$. These parameters can be combined to give three non-dimensional numbers that govern the flow: a Reynolds number for the basic rotation $Re = \Omega R^2/\nu$, the aspect ratio of the cylinder $\Lambda = H/R$, and the rotation ratio s. These can also be combined to give a Reynolds number for the differential rotation $Re_s = \Lambda(s-1)Re$. We see that when $s = 1$, $Re_s = 0$ and the system is in solid-body rotation. Numerical solutions over a wide range in $s \in [-3, 3]$ are presented for various values of Re and Λ, with particular emphasis placed on $Re = 3 \times 10^3$ and $\Lambda = 0.5$ at which values a wide

range of the dynamics are revealed. The solutions with $Re = 3 \times 10^3$ and $s \geqslant -2.65$ are steady, and over a small range $-0.893 \leqslant s \leqslant -0.853$ we have found two stable steady solutions. The two solutions are distinguished by where the shear layer that is formed from the separation of the endwall boundary layer on the counter-rotating top terminates. For one class of solutions it terminates in the boundary layer on the bottom endwall and for the other it re-attaches to the counter-rotating disk. For Re_s small, we find that the flow is a small perturbation of the solid-body rotation flow, and is well described by the considerations of Batchelor (1951). For strong counter-rotation ($s < -2.7$), we find a Hopf bifurcation to a limit cycle flow followed very rapidly, with further counter-rotation, by secondary Hopf bifurcation to a two-torus flow as well as behaviour symptomatic of homoclinicity/hetroclinicity of the Šil'nikov type (Šil'nikov 1965), as the separated shear layer becomes unstable. We also present some results at higher Re, but with Re_s small that coincide more closely with the parameter regimes considered by Hart & Kittelman (1996). For these, unsteadiness sets in for small positive $s - 1$ as a result of sidewall layer instability.

In the following section we formulate the problem and briefly describe the method of its numerical solution. In §3 we consider the flow in the Stokes limit $Re \to 0$, but with finite s, to gain an understanding of the basic structure of the flow. Section 4 describes the steady flows that result for co-rotation of the top and how these relate to the similarity solutions. Section 5 considers the counter-rotating top case, with an emphasis on the steady flows. Section 6 describes the onset of axisymmetric instabilities in the counter-rotating top case, and §7 considers the instability of the sidewall boundary layer for a co-rotating top.

2. Problem formulation and its numerical solution

Consider the flow in a completely filled cylinder of fluid with kinematic viscosity ν of radius R and height H with the bottom and sidewall rotating at a constant angular speed Ω and driven by the rotation of its top at angular speed $s\Omega$. Using R as the length scale and $1/\Omega$ as the time scale, the flow is governed by three non-dimensional parameters: $Re = \Omega R^2/\nu$, the Reynolds number for the basic rotation, $\Lambda = H/R$, the aspect ratio, and s, the rotation ratio.

These can be combined to give other common non-dimensional groups, such as the Ekman number Ek, where $Ek^{-1} = \Lambda^2 Re$, and the the Rossby number $Ro = s - 1$. A Reynolds number for the differential rotation in the enclosed cylinder may also be defined as $Re_s = \Lambda Ro Re$.

Here, we only consider the axisymmetric flow in order to gain an understanding of its basic features to facilitate the identification of the mechanisms responsible for its instability. The flow is governed by the axisymmetric Navier–Stokes equations that we write using a cylindrical polar coordinate system in the non-rotating frame (r, θ, z) with the corresponding velocity (u, v, w). We introduce the Stokes streamfunction ψ, where $u = -1/r\partial\psi/\partial z$ and $w = 1/r\partial\psi/\partial r$, and the circulation function $\Gamma = rv$ (angular momentum). Contours of ψ and Γ in a meridional plane give the cross-sections of streamsurfaces (streamlines) and vortex surfaces (vortex lines) in that plane. The azimuthal component of vorticity η is written in terms of ψ as

$$\nabla_*^2 \psi = -r\eta, \tag{2.1}$$

where

$$\nabla_*^2 = \frac{\partial^2}{\partial z^2} + \frac{\partial^2}{\partial r^2} - \frac{1}{r}\frac{\partial}{\partial r}.$$

The Navier–Stokes equations in terms of Γ, η, and ψ are

$$\mathrm{D}\Gamma = \frac{1}{Re}\nabla_*^2\Gamma, \tag{2.2}$$

$$\mathrm{D}\left(\frac{\eta}{r}\right) - \frac{\partial}{\partial z}\left(\frac{\Gamma^2}{r^4}\right) = \frac{1}{Re}\left(\nabla^2\left(\frac{\eta}{r}\right) + \frac{2}{r}\frac{\partial}{\partial r}\left(\frac{\eta}{r}\right)\right), \tag{2.3}$$

where

$$\mathrm{D} = \frac{\partial}{\partial t} - \frac{1}{r}\frac{\partial\psi}{\partial z}\frac{\partial}{\partial r} + \frac{1}{r}\frac{\partial\psi}{\partial r}\frac{\partial}{\partial z},$$

and

$$\nabla^2 = \frac{\partial^2}{\partial z^2} + \frac{\partial^2}{\partial r^2} + \frac{1}{r}\frac{\partial}{\partial r}.$$

The governing equations are actually solved in primative form, i.e. velocity–pressure, but the discussion of results is more natural in terms of ψ, η, and Γ. The numerical technique uses a spectral projection scheme designed specifically for axisymmetric systems in cylindrical polars (Lopez & Shen 1998). It uses a second-order projection scheme for time discretization and a new spectral-Galerkin approximation (Shen 1997) for the spatial discretization. Here, we use n Legendre polynomials in the axial and m Legendre polynomials in the radial direction. The spectral-Galerkin method is based on a variational formulation that naturally incorporates the coordinate singularity at the axis. The boundary conditions on the cylinder endwalls and sidewall are no-slip. Note that the differential rotation between the top and the sidewall leads to a discontinuity in v at the corner where they meet. This singularity is treated appropriately with a new procedure that produces mesh-independent approximations to the singular boundary condition to within any prescribed accuracy. The details of the scheme implementation and a detailed comparison with a standard second-order in time and space finite-difference scheme for a problem related to the present one is given in Lopez & Shen (1998). A key feature of the scheme, particularly useful for time-accurate solutions, is that it is absolutely stable in that the time step δt for stability of the scheme does not depend on the spatial resolution used; it does however depend on the Reynolds number (in this flow, the appropriate Reynolds number is $Re_s = \Lambda RoRe$). Extensive tests have been performed to ensure solutions that are independent of space and time discretizations in the present study guided by a similar study for a related problem in Lopez & Shen (1998). Table 1 lists the time and space resolutions used in the various parameter ranges reported here.

Two classes of initial conditions have been considered. For most cases, the computations were started impulsively from a state of solid-body rotation and evolved in time until either a steady state or a time-periodic state were reached (for non-periodic cases, the system was evolved for long times). The other type of initial condition corresponds to a continuation, where a steady state at one value of the parameter (usually s) is used as the initial condition for an impulsive small change in the parameter. This second type of initial condition was used to follow particular solution branches in parameter regimes where multiple solutions exist.

3. Low-*Re* limit

The matching between the endwall layers and the sidewall layer is non-trivial, regardless of the aspect ratio of the system. In their study of confined differentially rotating systems, Mundt, Hart & Ohlsen (1995) conclude that the presence of the

A	Re	s	δt	n	m
0.5	6×10^4	$0.6 \leqslant s \leqslant 1.05$	1.0×10^{-2}	128	256
0.5	6×10^4	$s = 1.20$	7.5×10^{-3}	128	256
0.5	6×10^4	$s = 1.35$	5.0×10^{-3}	128	256
0.5	6×10^4	$s = 1.50$	2.5×10^{-3}	128	256
0.5	3×10^3	$0.6 \leqslant s \leqslant 2.0$	1.0×10^{-2}	64	128
0.5	3×10^3	$-2.0 \leqslant s \leqslant -0.65$	5.0×10^{-3}	64	128
0.5	3×10^3	$s = 3.0,\ -3.0 \leqslant s \leqslant -2.2$	2.5×10^{-3}	64	128
0.5	1×10^3	$-1.5 \leqslant s \leqslant 2.0$	5.0×10^{-2}	48	96
0.5	1×10^3	$s = 2.5,\ s = -2.0$	2.5×10^{-2}	48	96
0.5	1×10^3	$s = 3.0,\ -2.5 \leqslant s \leqslant -2.25$	1.25×10^{-2}	48	96
0.5	1×10^3	$-3.0 \leqslant s \leqslant -2.75$	6.25×10^{-3}	48	96
0.25	1×10^3	$-1.7 \leqslant s \leqslant 2.2$	5.0×10^{-2}	24	96
0.25	1×10^3	$s = 2.4,\ -1.9 \leqslant s \leqslant -1.8$	2.5×10^{-2}	24	96
0.25	1×10^3	$2.6 \leqslant s \leqslant 3.0,\ -2.5 \leqslant s \leqslant -2.0$	1.25×10^{-2}	24	96
0.25	1×10^3	$-3.0 \leqslant s \leqslant -2.6$	6.25×10^{-3}	24	96
0.125	1×10^3	$-0.5 \leqslant s \leqslant 1.2$	5.0×10^{-2}	24	96
0.5	5×10^2	$-0.6 \leqslant s \leqslant 1.2$	5.0×10^{-2}	32	64
0.5	3×10^2	$-0.6 \leqslant s \leqslant 1.2$	5.0×10^{-2}	32	64

TABLE 1. Spatial and temporal resolution used

viscous sidewall boundary layer generally appears to have a global effect on the dynamics, and its inclusion is essential for accurately simulating the laboratory flows. Although Brady & Durlofsky (1987) are correct that for an inviscid sidewall it makes no difference, to a first approximation, whether it is rotating or not, when the sidewall is no-slip the state of its rotation has a global effect. The singular corners where the endwalls and sidewall meet are a source or sink for the vortex lines, as are the rotating endwalls. The global structure of the flow, for all Re, depends critically on whether the sidewall rotates or not. We illustrate this in the case of Stokes flow ($Re \to 0$), where a closed-form solution exists (Khalili & Rath 1994), in figure 1 where the vortex lines (contours of $\Gamma = rv$) are drawn when the sidewall co-rotates with the bottom (figure 1*a–d*) and when it is stationary (figure 1*e–h*) for $s = 2$, 1, 0, and -1. In this study, to investigate the effect of a differentially rotating top on a rotating system, we have the sidewall co-rotating with the bottom endwall. One of the main implications of this is that there is only one value of s for which the system has reflection symmetry about the midplane, Z_2-symmetry, that being $s = 1$. If the sidewall were stationary, then Z_2-symmetry would be preserved by the geometry for $s = \pm 1$.

The flow at low Re is steady and unique. However, as Re is increased a secondary meridional circulation is produced by the centrifuging of fluid adjacent to the rotating endwalls. This secondary flow interacts with the primary flow leading to further nonlinear interactions as the vortex lines are stretched and bent. As will be further described in the following sections, various instabilities arise as a result, leading to non-uniqueness and unsteady behaviour. In their inviscid treatment of the sidewall, Brady & Durlofsky (1987) note that for counter-rotation ($s < 0$), especially for large Re, there is some degree of ambiguity regarding the behaviour of the flow near the sidewall, but claim that the details are not important as the effects were found to be local. We find however, that the presence of a no-slip sidewall is felt globally.

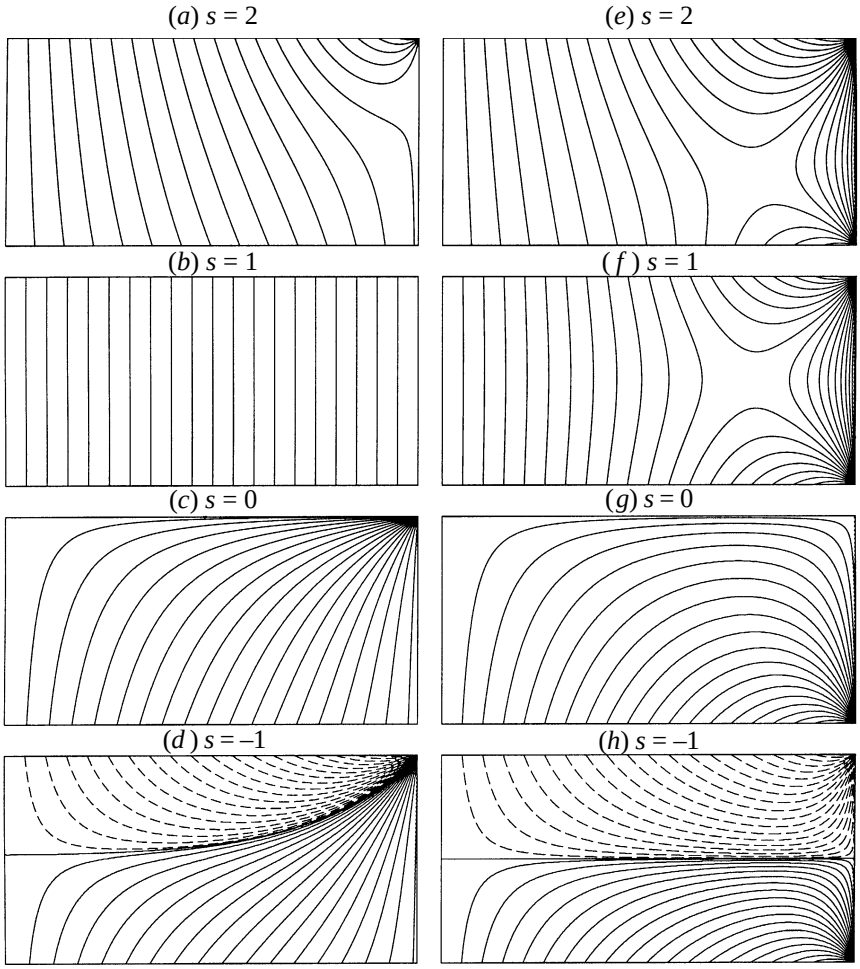

FIGURE 1. Contours of Γ for the Stokes flow ($Re = 0$) between rotating disks with the top disk rotating s times the rate of the bottom disk, with the sidewall co-rotating with the bottom (*a–d*) and with the sidewall stationary (*e–h*). Contour levels are set so that $\text{level}_i = C(i/20)^2$, $i = 1 \rightarrow 20$, where $C = \pm 2$, positive (negative) contours are solid (broken) and the zero contour is also drawn solid. In all contour plots, the left boundary is the axis ($r = 0$), the right boundary is the cylinder sidewall ($r = 1$), and the top ($z = \Lambda$) and bottom ($z = 0$) boundaries are the rotating disks.

4. Co-rotation of the top disk

For $Re \sim O(10^3)$ and $\Lambda = 0.5$, the dynamics of the flow are effectively summarized in figure 2, which is a plot of $v_{\text{mid}} = v(0.5, 0.5\Lambda)$ at steady state vs. s for $Re = 10^3$ and 3×10^3. The dotted line is half the arithmetic mean of the angular velocities of the top and bottom disks. This line is tangent to the v_{mid} vs. s curve at $s = 1$, where the flow is in solid-body rotation. Lance & Rogers (1962) have considered the flows between infinite disks, i.e. no influence of the sidewall, by numerically solving the similarity form of the steady axisymmetric Navier–Stokes equations. They found that at high Reynolds numbers the main core of the flow is in solid-body rotation with a slow drift in the axial direction from the slower to the faster disk. Furthermore, they observed that the fluid between the two disks rotates at a rate intermediate between those of the top and bottom disks and that the axial flow out of the boundary

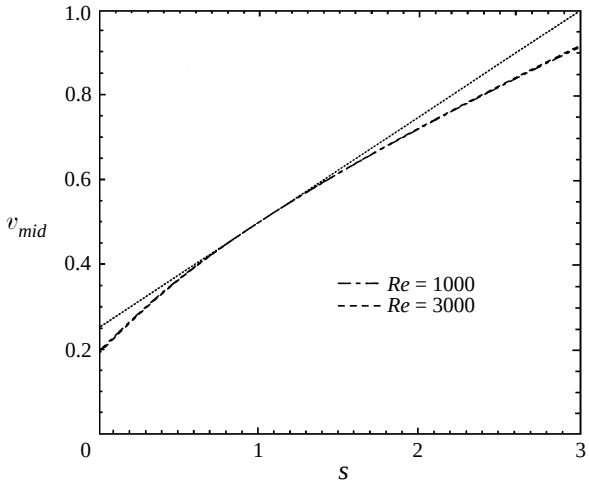

FIGURE 2. v_{mid} vs. s for $Re = 10^3$ and 3×10^3, and $\Lambda = 0.5$. The dotted line is half the arithmetic mean of the rotation rates of the two disks.

layer on the slow disk exactly matches the axial flow into the boundary layer on the faster disk. The rate of rotation of the bulk flow that achieves this 'detailed matching' deviates from one half the arithmetic mean of the angular velocities of the top and bottom disks as s in increased or decreased from 1. Rott & Lewellen (1967) present graphically this rotation rate for $0 \leqslant s \leqslant 1$ in their figure 6. The behaviour is in very good agreement with that shown in our figure 2. The discussion in Rott & Lewellen does not indicate to which Re the results correspond, but Lance & Rogers indicate that the system becomes asymptotically independent of Re, the asymptotic results typically being obtained by $Re \sim 10^3$ or lower for the range of s considered. The effects of a rotating no-slip wall were also approximately accounted for by Rott & Lewellen when the top is stationary ($s = 0$) using a momentum-integral method and looking for detailed matching. Their result agrees well with experimental measurements of Maxworthy (1964) for $Re = 2 \times 10^4$ and with numerical solutions of the Navier–Stokes equations over a range $10^3 \leqslant Re \leqslant 10^5$ (Lopez 1996). The results from the present spectral-projection numerical method also agree with the finite difference results presented in Lopez (1996).

The low-Re results from the previous section show that detailed matching is only achieved in the immediate neighbourhood of $s = 1$. As Re is increased, we find from our Navier–Stokes computations that detailed matching is achieved over an increasingly larger radial extent and for increasingly larger $|s-1|$. Figure 3 shows the streamfunction ψ, the azimuthal vorticity η, and the angular momentum Γ for $s = 3$, 1.5, 0.5, and 0, $Re = 3 \times 10^3$, and $\Lambda = 0.5$. This represents a large deviation from the state of solid-body rotation, but as indicated both by the contours in figure 3 and the curve v_{mid} vs. s in figure 2, the basic features of these flows are qualitatively consistent with the similarity considerations of disks of infinite radius. The boundary layers on the disks and the sidewall are well demarcated by the regions of non-zero η; the interior is in solid-body rotation with a slow axial drift from the slow to the fast disk; away from the sidewall boundary layer there is detailed matching with the streamlines (ψ) and the vortex lines (Γ) both being independent of z; the radial flow in the boundary layer of the fast disk is outwards, and inwards for the slow disk;

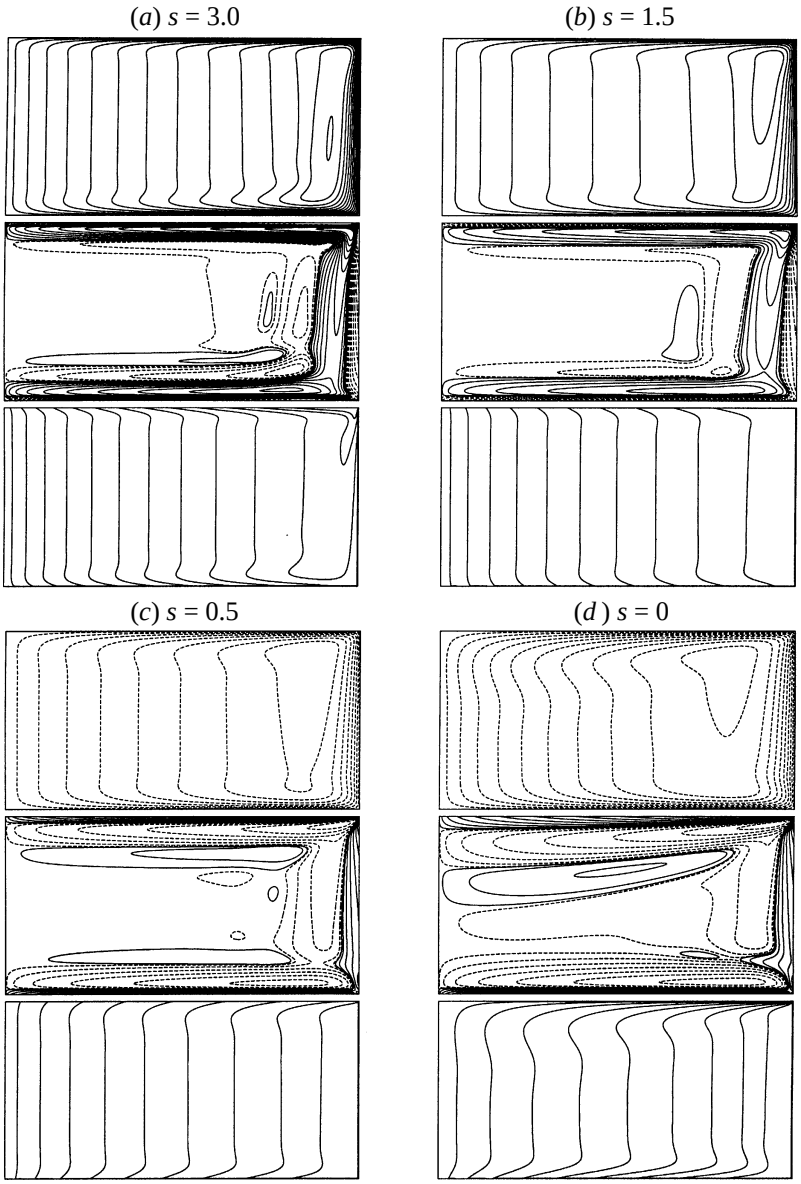

FIGURE 3. Contours of ψ (top), η (middle) and Γ (bottom) for $Re = 3 \times 10^3$, $\Lambda = 0.5$ and s as indicated. Contour levels are set so that $\text{level}_i = C(i/15)^3$, $i = 1 \rightarrow 15$, where $C = \pm 0.01$ for ψ, $C = \pm 25$ for η, and $C = \pm 3$ for Γ; positive (negative) contours are solid (broken).

both the streamlines and the vortex lines have oscillations as they leave or enter the disk boundary layers, the oscillations near the slower disk being greater.

Figure 4(a) gives radial profiles of v/r at $z = 0.5\Lambda$ for a large range in Re and for various s near $s = 1$. This figure is indicative of the extent to which the flow is in solid-body rotation and gives a clear indication of the transition between the rotation rate of the interior and the rotation rate of the sidewall. Further, it indicates that the rotation rate of the interior is independent of Re for $Re \geqslant 500$, as suggested by the results of Lance & Rogers (1962). Figure 4(b) gives radial profiles of v/r with

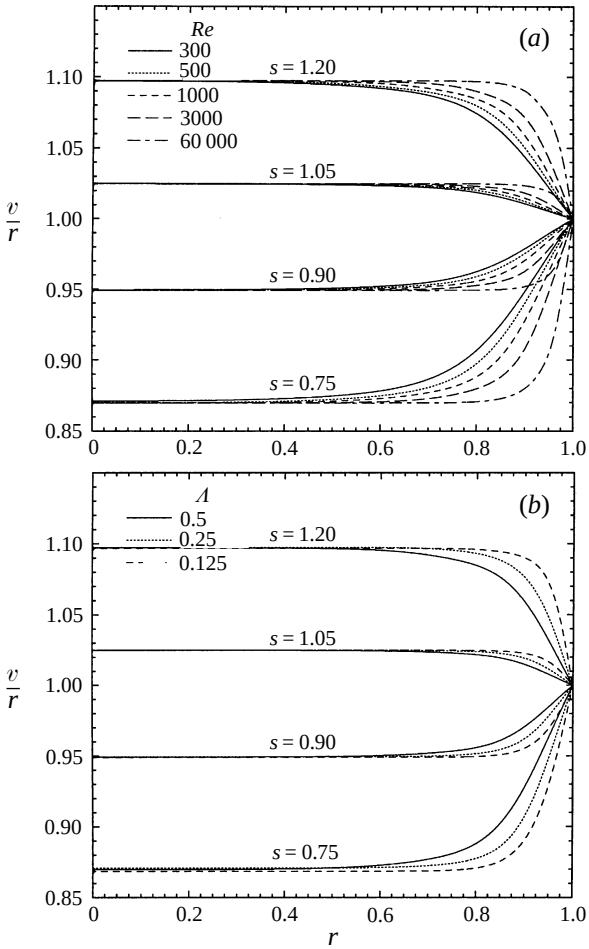

FIGURE 4. Radial profiles of v/r at (*a*) $z = 0.5\Lambda$ for various Re and (*b*) $Re = 10^3$ for various Λ, and s as indicated.

$Re = 10^3$ and $\Lambda = 0.5$, 0.25, and 0.125. From this figure, we see that the rotation rate of the interior is also independent of Λ, so it is independent of H, R, and v and is determined solely by s; this is true for co-rotation and when the boundary layers are stable and sufficiently well defined so that the interior is essentially irrotational. When this is all true, then the suggestion of Batchelor (1951) and Lance & Rogers (1962), based on considerations of co-rotating disks of infinite radius, that the interior flow consists of matching solutions of single disk flows, also holds in the case of finite-radius shrouded disks. Whereas the thickness of the boundary layers on the disks is independent of Λ (e.g. see figure 5, where η for various Λ is given), the sidewall boundary layer thickness varies with Λ (figure 4), i.e. the separation between the disks is a relevant length scale for the sidewall but not for the disk boundary layers.

Section 7 describes how the sidewall layer becomes unstable as both s and Re are increased: for $s > 1$ the interior is rotating faster than the sidewall and for larger Re, the adjustment is over a smaller radial distance. For $s < 1$, but positive, the sidewall layer is centrifugally stable. From the contours of η in figure 3, it is clear that the

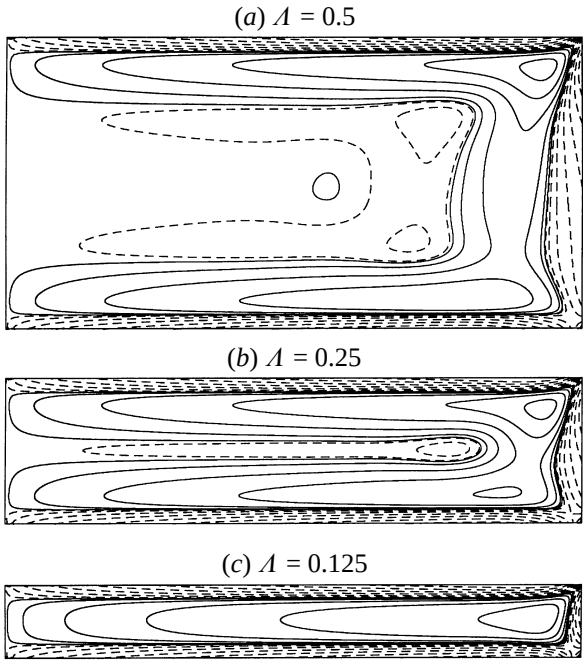

FIGURE 5. Contours of η for $Re = 10^3$, $s = 1.2$, and Λ as indicated. Contour levels are set as in figure 3.

radial profile of η as it approaches the sidewall is oscillatory (and hence has inflection points) for $s > 1$ and is monotonic for $s < 1$.

5. Counter-rotation of the top disk

In the previous section, we found that for co-rotation the numerical solutions for the shrouded cylinder agree quite well with the similarity solutions for infinite-radius disks, so long as the sidewall layer does not become unstable. For counter-rotation, we do not find this level of correspondence with the similarity solutions. It is interesting that for counter-rotations with $s < -0.15$ similarity considerations of the infinite unbounded disk have problems with non-uniqueness and convergence (Zandbergen & Dijkstra 1977). Dijkstra & van Heijst (1983) suggest that the presence of a sidewall eliminates the non-uniqueness in the similarity solutions. However, the Navier–Stokes computations suggest that similarity is not appropriate for $s < 0$, as there are many sources of instabilities and even when the flow is steady, it is not close to being self-similar, unlike the situation for $s > 0$ noted in the previous section.

In his consideration of the flow between counter-rotating disks of infinite radius, Batchelor (1951) notes that there exists a plane, a transition layer, where $v = 0$ between the two disks. In describing their numerical solutions of the similarity equations for flow between a rotating disk and fluid in solid-body rotation where the ratio of the rotation of the fluid to that of the disk is s^*, Rogers & Lance (1960) note that when $s^* > 0$, the solutions converge to physically sensible results. However, for $s^* < 0$, they observed that the boundary layer on the disk seemed to move away from the disk and that large shears appeared in the body of the fluid. Further, when $s^* < -0.2$, they were unable to obtain steady solutions unless they imposed suction at the disk

to prevent the boundary layer from leaving the disk. For $-0.2 < s^* < 0$, they obtain steady self-similar solutions, but comment that they appear anomalous.

The difficulties encountered in the similarity formulation for $s < 0$ associated with the apparent lifting of the boundary layer are paralleled in the flows between shrouded counter-rotating disks. Dijkstra & van Heijst (1983) observed in their computations that the boundary layer flow on the slower disk develops a stagnation ring and that the boundary layer separates, forming a shear layer along which the velocity is jet-like. They also matched the radial location of this stagnation (separation) ring from their Navier–Stokes computations with experimental measurements over the range $-1 < s < 0$. For their small-aspect-ratio flows ($A = 0.07$), they found that the meridional shear layer ($\psi = 0$) and the azimuthal transition layer ($\Gamma = 0$) separating the counter-rotating bodies of fluid, did not coincide. In our computations with $A = 0.5$ and with effective Reynolds numbers in the same range as Dijkstra & van Heijst, we find that the two shear layers, $\psi = 0$ and $\Gamma = 0$, coincide in the interior outside the disk and sidewall boundary layers.

In contrast to the co-rotating case, when the disks counter-rotate the distance between them has a profound global and local influence on the flow. Figure 6 gives the flows for $Re = 10^3$ and $s = -0.5$ with $A = 0.5$, 0.25, and 0.125. The most striking global effect of the aspect ratio is on the separation of the boundary layer on the counter-rotating disk. At the larger A, the layer separates forming a free shear layer that enters into the interior. This separation layer consists of shear in the meridional flow ($\psi = 0$) and in the interior this layer coincides with the azimuthal transition layer ($\Gamma = 0$). For $A = 0.25$, the interior region is much reduced and the $\psi = 0$ separation does not coincide with the $\Gamma = 0$ separation anywhere. As A is further reduced to 0.125, the boundary layers on the two disks are virtually merged together and there is no $\psi = 0$ separation. On a more local level, we find that the boundary layer on the bottom disk has a boundary layer whose thickness varies with A. This is in contrast to the co-rotating case where the thickness is independent of A. So, in the counter-rotating case there is a strong coupling between the two disks, their proximity strongly influencing the qualitative nature of the flow in the boundary layers of both disks, whereas for co-rotation the coupling is much weaker. In that case the coupling only enforces a detailed matching between the two, and so long as there is sufficient separation so that distinct boundary layers are formed, the distance separating the two plays essentially no role in the nature of the flow.

Dijkstra & van Heijst (1983) were unable to get reliable results in the range $-1 \leqslant s < -0.825$. Now we present steady results for $-2.265 \leqslant s < 0$ with $Re = 3 \times 10^3$ and $A = 0.5$, these being on two distinct solution branches distinguished by the fate of the separated shear layer. In the following section, flows with $s < -2.265$ are considered where the shear layer is observed to become unstable.

We have continued the solution branch described in §4 to negative s for both $Re = 10^3$ and 3×10^3 with $A = 0.5$ and $Re = 10^3$ with $A = 0.25$. We have already seen in figure 3(*d*) for $s = 0$ that the boundary layer on the stationary disk has thickened considerably in comparison with the layer for $s > 0$, and is thickest as $r \to 0$. As soon as s becomes negative, Γ in the region closest to the counter-rotating disk also becomes negative, thus creating an azimuthal transition layer. This layer originates at the singular corner where the sidewall and counter-rotating disk meet, and terminates somewhere on the axis. For small $|s|$, this layer resides entirely within the counter-rotating disk's boundary layer (see figure 7*a* for $s = -0.15$, $Re = 3 \times 10^3$, $A = 0.5$). For $s \approx -0.2$, the azimuthal transition layer is not wholly contained within the disk boundary layer, but leaves it at a small r (as also observed by Dijkstra &

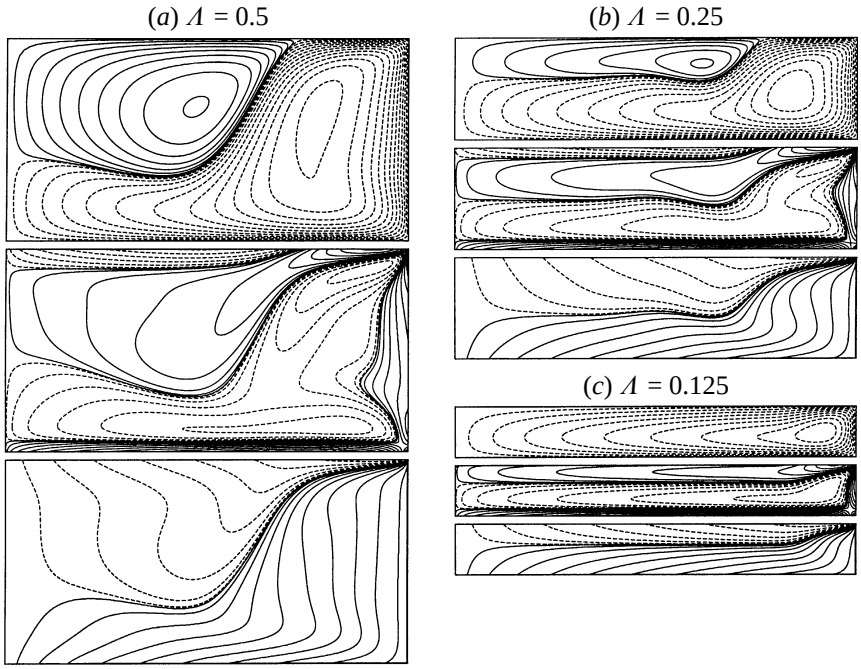

FIGURE 6. Contours of ψ (top), η (middle), and Γ (bottom) for $Re = 10^3$, $s = -0.5$, and Λ as indicated. Contour levels are set as in figure 3.

van Heijst 1983) and the meridional flow also separates, forming a stagnation ring on the disk and the meridional shear layer. The $\psi = 0$ line in figure 7(*b*) for $s = -0.25$, $Re = 3 \times 10^3$, and $\Lambda = 0.5$ clearly demarcates this shear layer. For $s > -0.3$ and $Re = 3 \times 10^3$, $\Lambda = 0.5$, the two layers terminate on the axis, yet for stronger counter-rotation they terminate in the boundary layer on the bottom disk. This behaviour is illustrated in figures 7(*c*) and 7(*d*) for $s = -0.5$ and $s = -0.75$ with $Re = 3 \times 10^3$ and $\Lambda = 0.5$.

For larger $|s|$ and Re, the meridional shear layer becomes narrower and more jet-like; it advects the vortex lines with it locally, so that the azimuthal transition layer develops shear in the azimuthal velocity. This shear, for sufficiently large $|s|$ and Re, could lead to azimuthal symmetry breaking. The inclination of the layers to the rotation axis can also be expected to play a role in the symmetry breaking. These important aspects of the flow dynamics are deferred to a future investigation where non-axisymmetric flows are considered.

Figure 8 gives v_{mid} vs. s for counter-rotation with $Re = 10^3$ and 3×10^3 with $\Lambda = 0.5$ and $Re = 10^3$ with $\Lambda = 0.25$, continuing the curves in figure 2 to negative s. For $-0.893 \leqslant s \leqslant -0.853$, depending on the initial conditions, the system with $Re = 3 \times 10^3$ and $\Lambda = 0.5$ may evolve to one of two distinct steady states. Contours of the flows at the ends of the hysteresis region are shown in figure 9. The structure of the sidewall boundary layers for the two branches is very similar, as is the structure of the shear layer near where the disk boundary layer separates. What distinguishes the two solutions is where their shear layers terminate. For the branch 1 solutions, it terminates in the bottom disk's boundary layer, whereas for the branch 2 solutions, the shear layer re-attaches itself to the boundary layer of the disk from which it separated. It is also apparent that the two branches are connected by an unstable

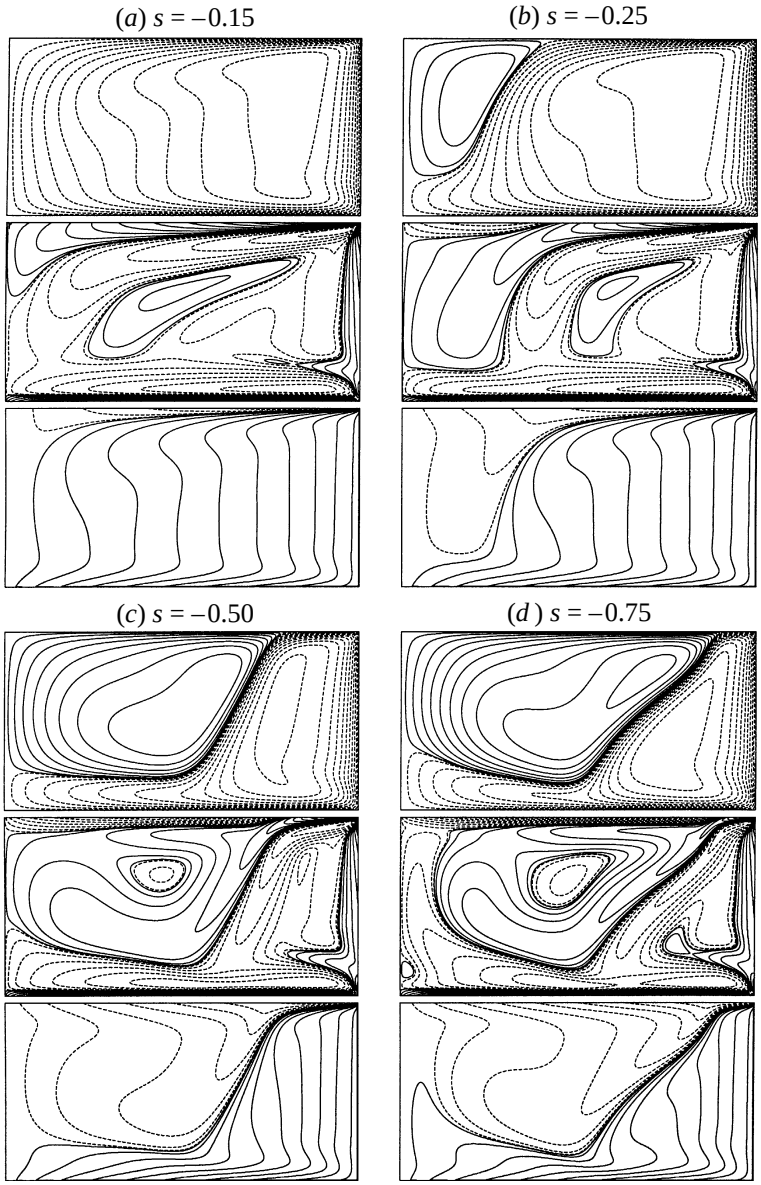

FIGURE 7. Contours of ψ (top), η (middle) and Γ (bottom) for $Re = 3 \times 10^3$, $\Lambda = 0.5$ and s as indicated. Contour levels are set as in figure 3.

branch. The three solutions originate at a cusp at a lower Re; for $Re = 10^3$ and $\Lambda = 0.5$, we see from figure 8 that there are no folds and that the solution undergoes a smooth transition as s is reduced. When viewed as a solution manifold in Re–s, all the steady solutions found are on the one solution manifold that has a fold (see schematic in figure 10). Similar folded solution manifolds have been identified in other swirling flows (Beran & Culik 1992; Lopez 1994). At low Re, the boundary layers are quite diffuse as is the separated shear layer.

For $s < -1.05$ with $Re = 10^3$ and 3×10^3, and $\Lambda = 0.5$ the meridional shear layer ($\psi = 0$) no longer separates from the counter-rotating endwall but instead separates

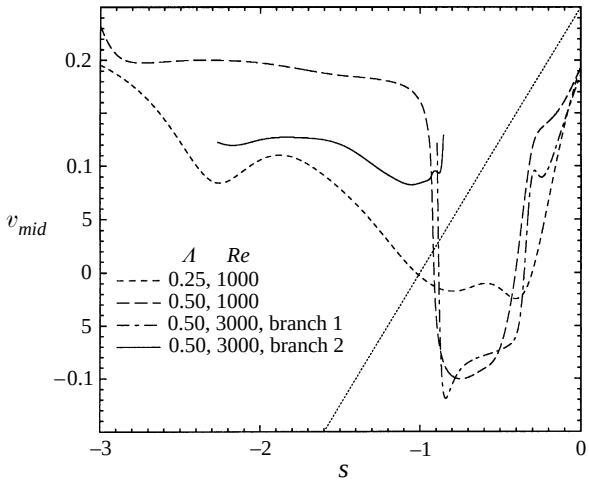

FIGURE 8. v_{mid} vs. s for Re and Λ as indicated. The dotted line is half the arithmetic mean of the rotation rates of the two disks.

from the sidewall. Recall that the azimuthal transition layer ($\Gamma = 0$) separates at the singular corner ($r = 1$, $z = \Lambda$) for $s < 0$ and all Re and Λ. This qualitative change in the solution is smooth and continuous: for $Re = 10^3$ it occurs along the only solution branch that has been found, and for $Re = 3 \times 10^3$ it occurs on branch 2 for stronger counter-rotation than that where the fold with hysteresis occurs. The smoothness of the transition is indicated in the v_{mid} vs. s curves (figure 8) and verified by the smooth and continuous changes in ψ, η, and Γ through the transition. Following the transition, i.e. from separation on the counter-rotating endwall to separation on the sidewall, there is a flattening of the v_{mid} variation with s and it has a strong dependence on Re and Λ.

Figure 11 gives the steady flows for $s = -1$ and -2 and $Re = 10^3$ and 3×10^3. For the same s, the region of fluid that is counter-rotating is thinner for the larger Re. This is a direct consequence of the rotating sidewall which attempts to keep the interior flow in solid-body rotation and is more successful in doing so as Re increases (until instabilities set in). One would not expect this to be the case if the sidewall were stationary. For $Re = 3 \times 10^3$, the meridional shear layer becomes unstable with $s < -2.265$. Some details of this instability are given in the following section. However, for $Re = 10^3$ viscosity suppresses this instability and the flow remains steady for the largest counter-rotation considered ($s = -3.0$). The steady solution at $s = -3.0$, $Re = 10^3$ is given in figure 12, along with an instantaneous view of the unsteady flow at $s = -3.0$, $Re = 3 \times 10^3$.

6. Instability of the separated shear layer

We have investigated the separated shear layer in some detail only for $Re = 3 \times 10^3$ and $\Lambda = 0.5$. It should be noted that these flows are governed by three parameters, s, Re, and Λ, and so a full appreciation of their dynamics requires variations in all three. Low-dimensional dynamical systems governed by three parameters are considerably more complicated than those governed by only one or two. We shall show behaviour that is suggestive of such low-dimensional systems, but a rigorous connection awaits further work.

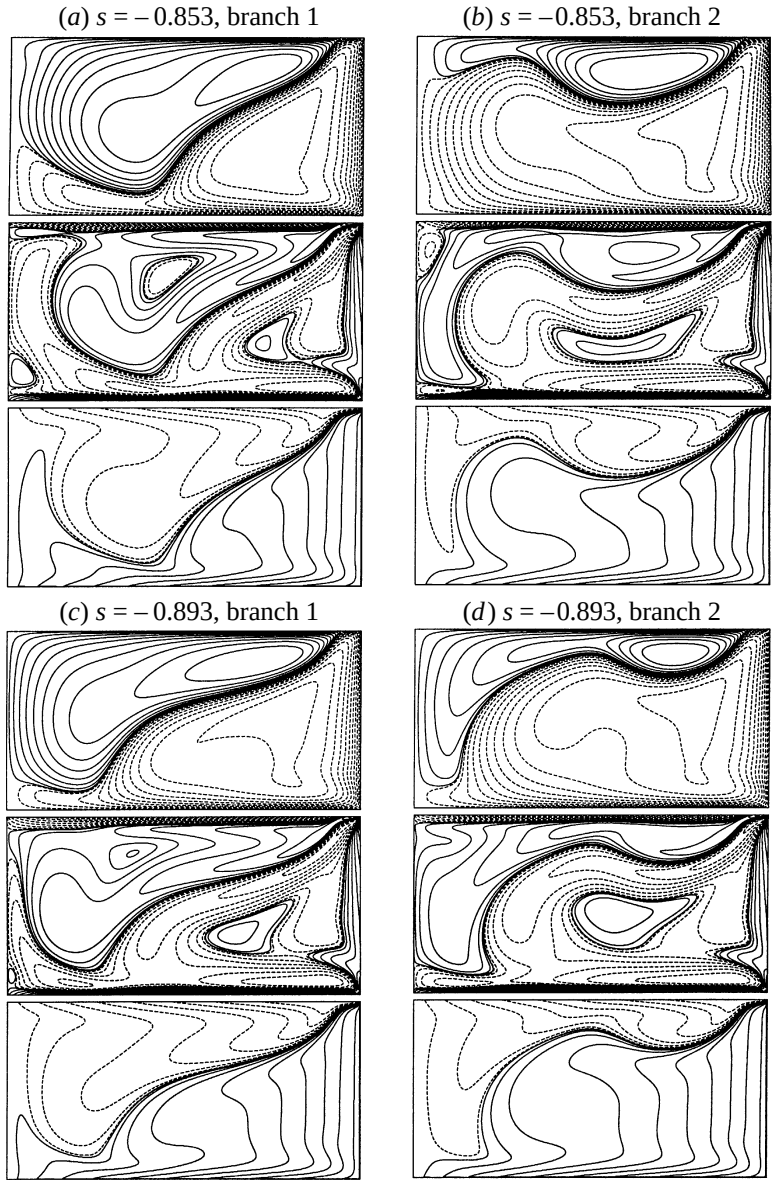

FIGURE 9. Contours of ψ (top), η (middle) and Γ (bottom) for $Re = 3 \times 10^3$, $A = 0.5$ and s as indicated at the two ends of the hysteresis range. Contour levels are set as in figure 3.

Figure 13 provides an overview of the development of the flow as s is reduced from -2.265. The phase diagrams in figure 13 are of v_{mid} vs. $\dot{v}_{\mathrm{mid}}$, its time rate of change. All the power spectral densities (PSD) are determined with at least 2^{18} samples of v_{min}, spaced $\delta t = 0.0025$ apart, which is the time-step used in these computations, and a Hamming window is utilized. One should note that the radius of the limit cycles in these figures is not a good measure of the amplitude of the oscillatory states. This is because the phase diagrams are constructed from a time series at a fixed physical location and the oscillations may or may not be large near this location. The oscillations correspond to an instability of the shear layer: how this influences

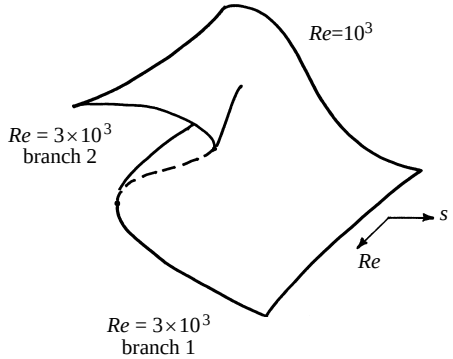

FIGURE 10. Schematic of the steady solution manifold in $Re - s$.

v_{mid} is not simple as the location of the shear layer varies with s. So, the amplitude information here, while accurate, is not useful for analysis of the dynamics. However, the frequency content of the temporal information is both accurate and relevant, and the resulting phase diagrams are useful diagnostics of the qualitative nature of the dynamics.

The steady flow described in §5 becomes unstable to a limit cycle flow for $s \approx -2.27$, and by $s = -2.325$ we have flow on a two-torus. The frequency of the limit cycle flow remains one of the frequencies of the two-torus flow. We shall denote this frequency ω_1 and note that it varies smoothly with s (we did not investigate its variation with either Re or A). The second frequency ω_2 does not vary with s as much as ω_1 does. For the range of s considered, the ratio ω_1/ω_2 varies between approximately 6 and 4, with the two frequencies alternately being commensurate and incommensurate as s is varied, showing evidence of frequency locking. As well, we find windows in s where the flow is periodic with its PSD consisting only of ω_1 and superharmonics. At $s = -2.400$, the flow is periodic and there is no signal corresponding to ω_2. At $s = -2.500$, the flow has ω_1 and ω_2 in an almost 4 : 1 ratio together with sidebands of the form $\omega_2 \pm n(\omega_1 - 4\omega_2)$, leading to complicated dynamics. At $s = -2.600$, the ratio ω_1/ω_2 is 4, the sidebands have disappeared, and the flow is once again periodic. For $s = -2.700$ and $s = -2.800$, the flow consists of two main signals ω_1 and ω_2 in an almost 4 : 1 ratio with the sidebands providing very low-frequency modulations. This is also evident from the short time sequence of v_{mid} provided in the figures. The time sequence for $s = -2.800$ clearly shows that the signal almost repeat itself approximately every 19.7 time units (corresponding to $\omega_2 \approx 0.05$), with four major oscillations over that period (corresponding to $\omega_1 \approx 4\omega_2$), but the signal is not precisely repeated. This is seen most clearly in the phase diagram and in the PSD where there are peaks at $\omega < \omega_2$. It is difficult to fully resolve the PSD here, even with a very long time series consisting of 2^{19} data points. However, some of the dynamics can be inferred from the phase diagram. The phase diagrams in figure 13 suggest a smooth development as s is reduced from -2.27 to -2.8, and we now explore this development by looking at the whole flow rather than the time series of one component of the velocity at one point in the flow.

The dynamics of the flow for $s < -2.27$ are essentially determined by the dynamics of the separated shear layer and its interactions with the boundary layers. For $s \approx -2.3$, the shear layer re-attaches itself to the boundary layer on the counter-rotating disk, as described in §5; however, for these values of s, it becomes unstable. We should point out again that the flow dynamics considered are restricted to the

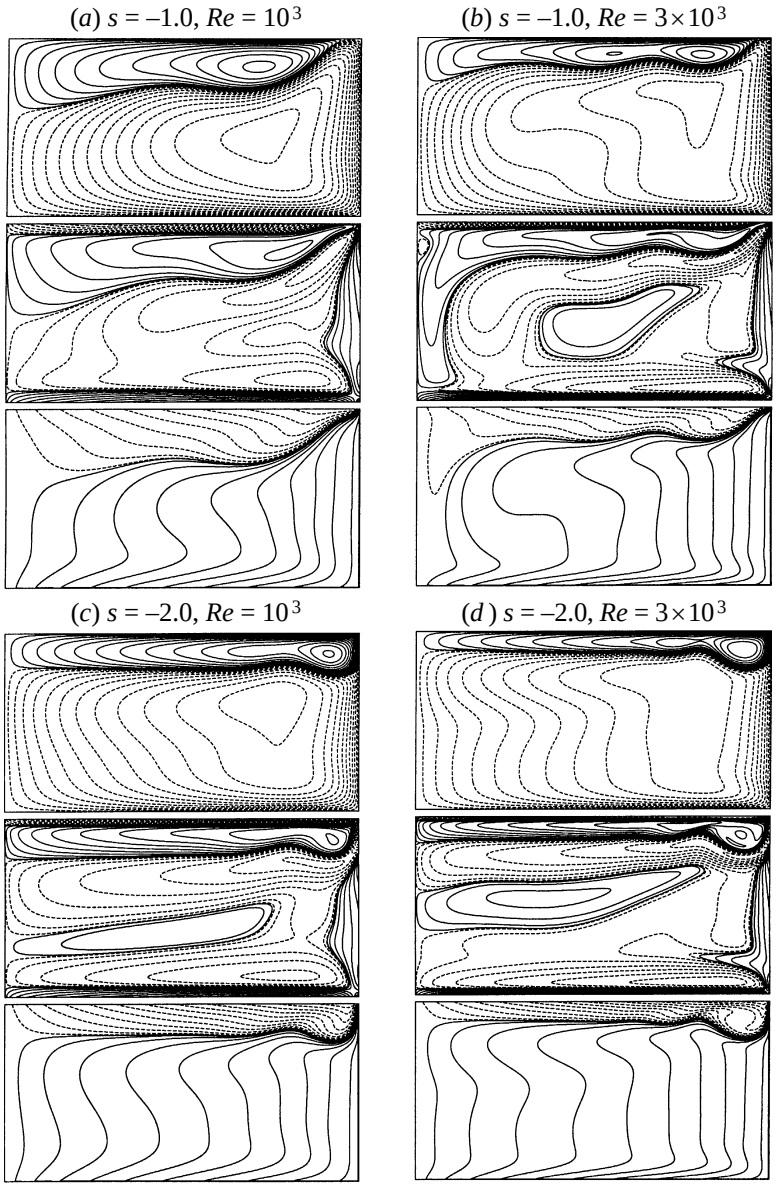

FIGURE 11. Contours of ψ (top), η (middle) and Γ (bottom) for $A = 0.5$ and s and Re as indicated. Contour levels are set as in figure 3.

space of axisymmetric flows, and that azimuthal instabilities are not considered in this initial study. Undoubtedly, in some parts of the (Re, A, s) parameter space, azimuthal symmetry breaking will take place, but this is an issue which has not yet been explored either numerically or experimentally for these flows. In the space of axisymmetric flows, the instability consists of waves originating in the shear layer and propagating radially inwards along the boundary layer. Figure 14 gives a sequence of snap-shots over one period, illustrating this ω_1 limit cycle behaviour. These waves are very effective in coupling the boundary layer flow on the counter-rotating disk with the interior flow and the flow in the sidewall layer, particularly for $r \sim 0.5$. For $s \sim -2.3$,

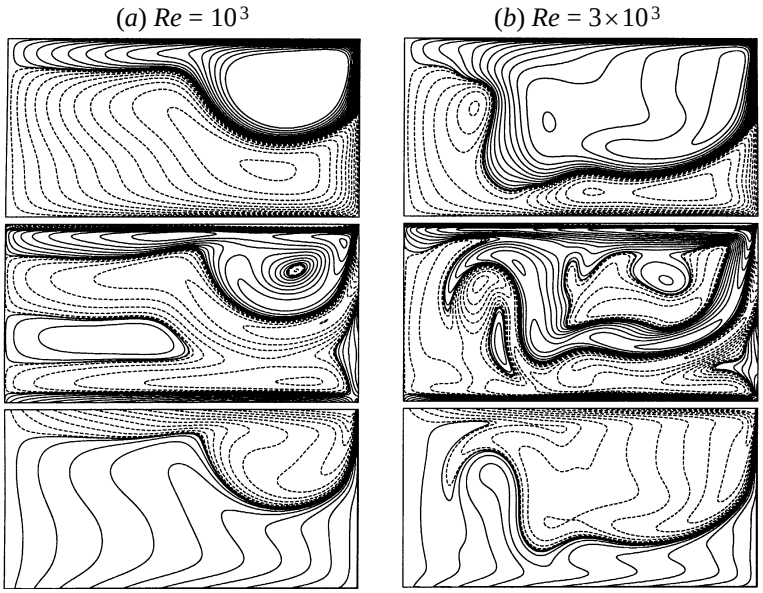

FIGURE 12. Contours of ψ (top), η (middle) and Γ (bottom) for $A = 0.5$, $s = -3.0$, and (*a*) $Re = 10^3$ (steady) and (*b*) $Re = 3 \times 10^3$ ('snap-shot' of unsteady flow). Contour levels are set as in figure 3.

the flow in the bottom disk boundary layer is not strongly influenced by these waves: it remains almost steady and not too far removed from its state at smaller $|s|$.

As s becomes more negative, the amplitude of the shear layer waves increases and their presence is felt on the bottom endwall boundary layer. This boundary layer is now essentially being periodically forced by the waves and it responds with its own characteristic time scale. This leads to the two-torus flow. For the range of s considered, the ratio of the two frequencies varies between approximately 4 and 6 in a continuous fashion. The flow with $s = -2.600$ is an example where the ratio is 4. Here, the shear layer flip-flops from one disk's boundary layer to the others in a regular fashion (see figure 15), thus creating a tight coupling between the two disk boundary layer flows. During this flip-flop mode, the shear layer responds much like a whip being cracked every period.

As s is further reduced, the shear layer separates further down the sidewall. For $s = -2.800$ the flip-flop mode described for $s = -2.600$ dominates, but now with the separation occurring further down the sidewall, the mean position of the shear layer is closer to the bottom endwall. As a result of this proximity, the shear layer is drawn into and remains within the boundary layer of the bottom endwall for some time. During this 'attached' phase, it still retains its own distinct identity and oscillates with the ω_1 frequency as it does when it resides in the interior. These oscillations are modulated and grow sufficiently for the shear layer to escape from the boundary layer and oscillate in the flip-flop mode in the interior. Eventually the boundary layer suction on the bottom disk builds up and the shear layer is once again attached to it. These sequences repeat fairly regularly, as evidenced in figure 13, but here we find sideband modulations of the modulation frequency ω_2 and the system is weakly chaotic. Comparing the phase diagrams for $s = -2.600$ and $s = -2.700$ (which are essentially pure flip-flop modes with the mean position of the shear layer in the interior) with that of $s = -2.800$, we find that at $s = -2.800$, the flow is in a

flip-flop mode a good deal of the time, but that it has a weak attraction to a location ($v_{\mathrm{mid}} \approx -0.3, \dot{v}_{\mathrm{mid}} \approx 0$). This location represents the state when the shear layer is primarily attached to the bottom endwall boundary layer.

By $s = -3.000$, the shear layer leaves the sidewall layer further down and is attached to the bottom endwall layer. It still oscillates within the boundary layer with a frequency ω_1 and leaves the bottom boundary layer at a radial location between $r = 0.25$ and $r = 0.5$. Superficially, the oscillatory state at $s = -3.000$ does not appear too different from that at $s = -2.600$ (compare figures 16 and 17 showing snap-shots of the $s = -3.000$ flow with figure 15 for $s = -2.600$), apart from the attachment of the shear layer to the bottom disk's boundary layer. However, a closer analysis reveals a number of qualitative differences.

Figure 18 shows a part of the time series, the PSD, and the phase diagram for $s = -3.000$. The time series reveals a very low-frequency modulation (period ≈ 145) on top of an oscillatory state with frequency ≈ 0.22, which is the frequency associated with the primary mode of oscillation of the shear layer ω_1 (compare with ω_1 for lower s from figure 13). On top of these are further modulations. The period 145 modulation tends to flip the oscillatory state between two states with mean $v_{\mathrm{mid}} \approx -0.15$ and ≈ -0.25. The flipping between these two states is evident both from the time series and the phase diagram. The snap-shots in figures 16 and 17 are sequences in each of the two states respectively. The open circles in the time series in figure 18 correspond to figure 16 and the open squares correspond to figure 17. It is difficult to get an impression of the differences between the two states from the snap-shots, but an animation using 80 frames over a period of 160 does serve to illustrate the dynamics. During the $v_{\mathrm{mid}} \approx -0.15$ phase, the shear layer oscillations tend to send waves radially in towards the axis along the bottom endwall boundary layer (much as it did when it was attached to the counter-rotating endwall layer at $s = -2.300$). These waves excite waves on the axis which primarily travel from top to bottom. When the flip occurs, the wave disturbances tend to travel not to the axis, but rather across the interior and then radially outwards along the boundary layer on the counter-rotating disk.

The weak unstable attractor observed at $s = -2.800$ corresponds to the attached mode at $s = -3.000$ with $v_{\mathrm{mid}} \approx -0.25$. The mode with $v_{\mathrm{mid}} \approx -0.15$ does not seem to have any corresponding mode at smaller $|s|$. The waves travelling on the counter-rotating boundary layer at $s = -2.300$ were in towards the axis, for $s = -3.000$ they are outwards. The mode at $s = -2.300$ is in essence a mirror image of the attached mode at $s = -3.000$ with $v_{\mathrm{mid}} \approx -0.25$ (compare the phase diagrams at $s = -2.5$ and $s = -2.8$ in figure 13).

The frequency of the period 145 modulation shown in figure 18 is quite small compared with the primary frequency: their ratio is approximately 32. At the lower s with the second ω_2 frequency present, the ratio ω_1/ω_2 was between 4 and 6. The low-frequency mode presumably appears via a secondary Hopf bifurcation, and with its associated frequency being much smaller than that typical of the system indicates that degeneracy may be playing a role. The types of degeneracies at low-frequency bifurcations studied by Davis & Rosenblat (1977) for a class of low-dimension ODEs or homoclinicity (hetroclinicity) of the Šil'nikov (1965) type may be of relevance. The state with mean $v_{\mathrm{mid}} \approx -0.25$ has characteristics of saddle-focus type: the trajectories spiral in towards it (the oscillatory sections from $v_{\mathrm{mid}} \approx -0.15$ to $v_{\mathrm{mid}} \approx -0.25$ in the time series) and are then rapidly and almost without oscillations ejected away from this region of phase space to the $v_{\mathrm{mid}} \approx -0.25$ region. The mode with $v_{\mathrm{mid}} \approx -0.25$ is weakly unstable and the flow evolves once again towards the saddle-focus at $v_{\mathrm{mid}} \approx -0.15$. This type of hetroclinic behaviour obviously occurs in a space of at

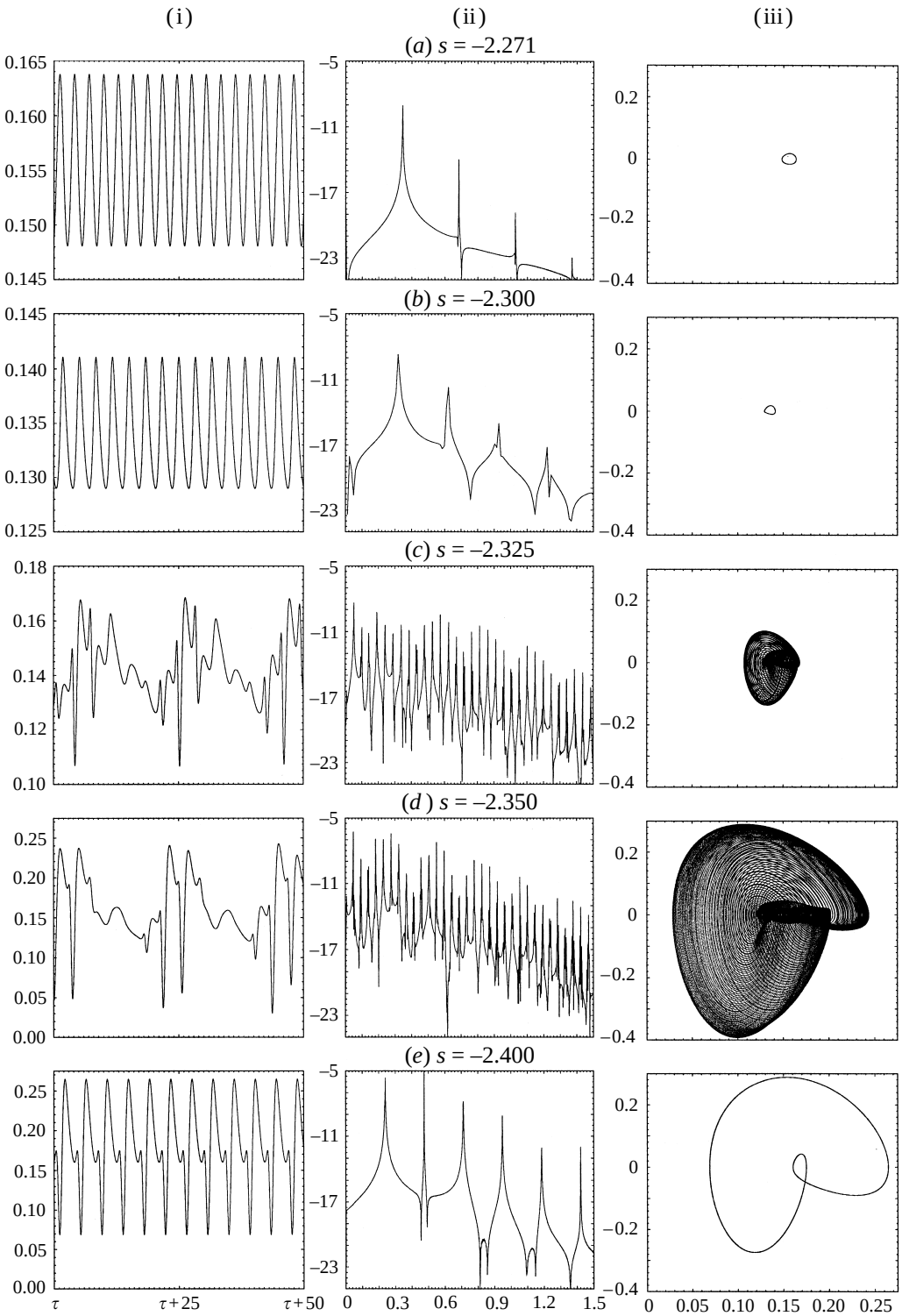

FIGURE 13(*a–e*). For caption see facing page.

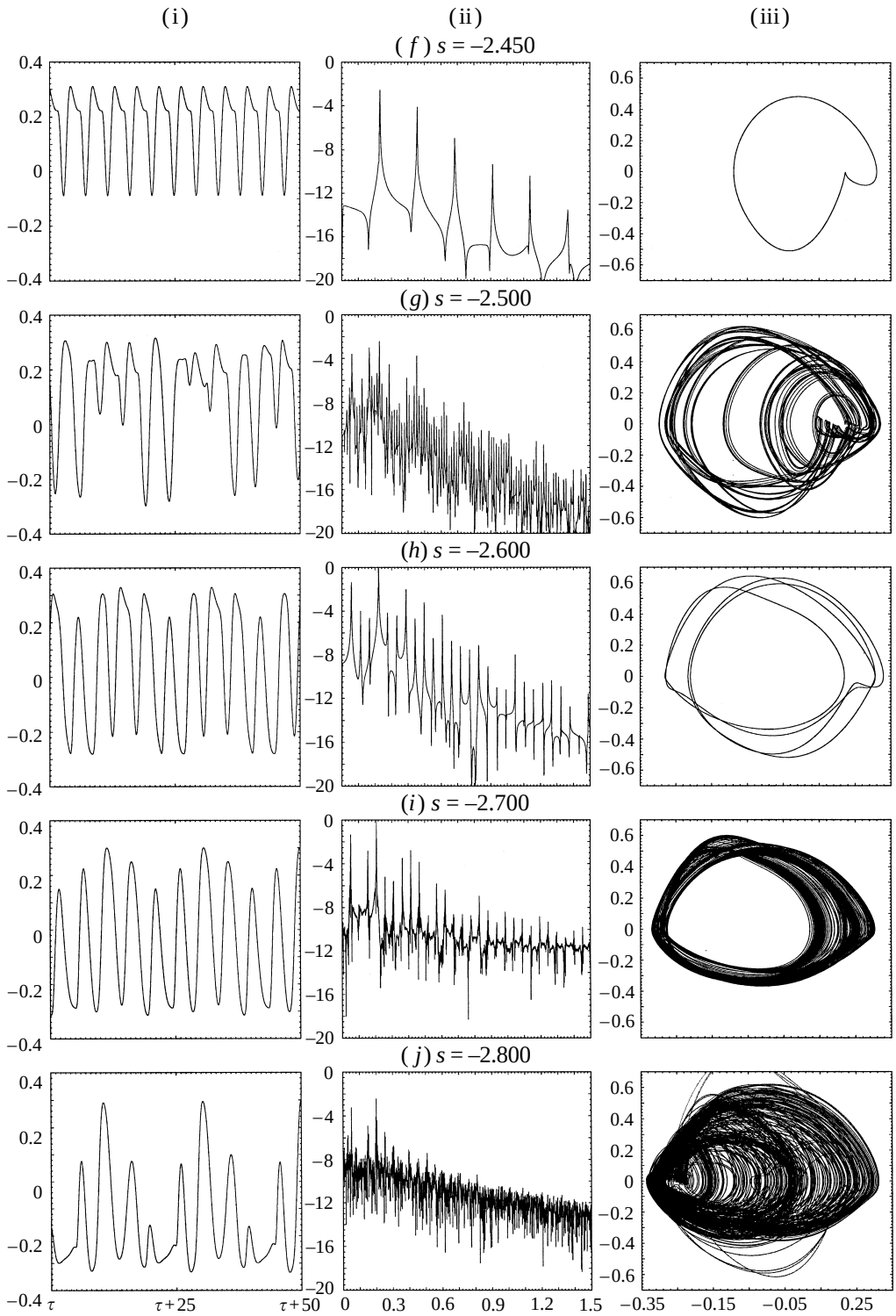

FIGURE 13. (i) Time series over 50 time units, (ii) log(PSD), and (iii) phase portrait of v_{mid} vs $\dot{v}_{\mathrm{mid}}$ for $Re = 3 \times 10^3$, $\Lambda = 0.5$, and s as indicated. The PSD were found with 2^{18} samples and 2^{19} for $s = -2.80$ and -2.90 spaced $\delta t = 0.0025$.

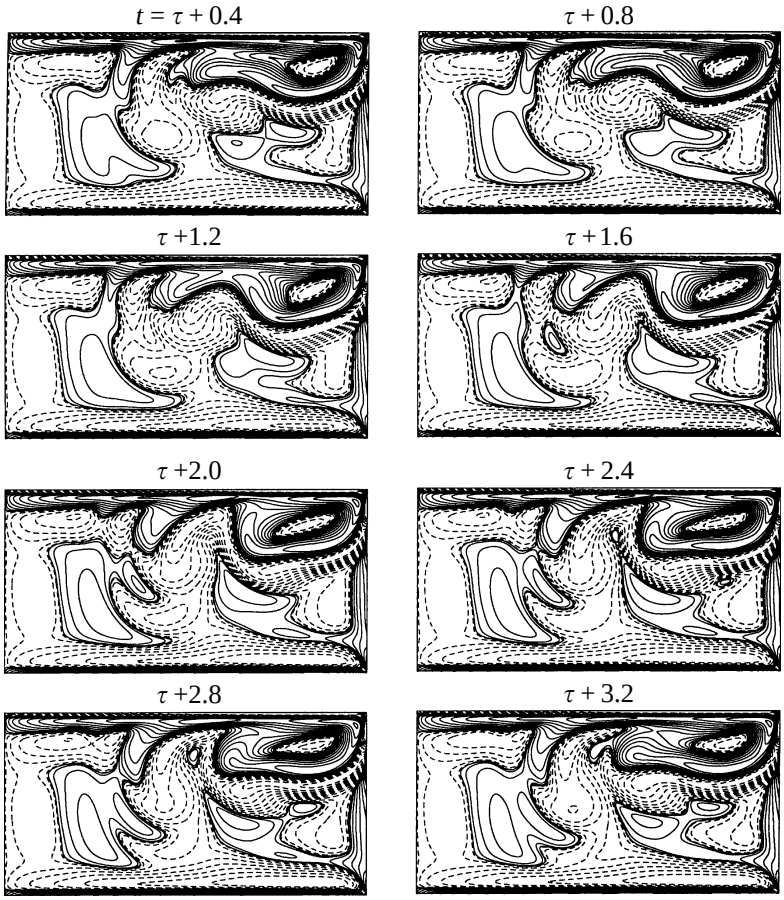

FIGURE 14. Contours of η for $Re = 3 \times 10^3$, $\Lambda = 0.5$ and $s = -2.300$ at times as indicated. Contour levels are set as in figure 3.

least three dimensions; the phase diagram presented in figure 18 is a projection onto the two-dimensional space of $(v_{\mathrm{mid}}, \dot{v}_{\mathrm{mid}})$.

While these aspects of the flow are interesting and deserve further investigations, we leave that for future investigation where azimuthal symmetry breaking will also be considered. From preliminary laboratory experiments (J. E. Hart, private communication), there is strong evidence that symmetry breaking also plays a role in determining the dynamics of these flows at sufficiently large counter-rotation. The symmetric solutions presented here lay the foundations for further investigations of the dynamics of these flows.

Axisymmetric computations of flow in a rotating annulus with a source/sink at the inner/outer radial boundaries by Crespo del Arco *et al.* (1996) revel a qualitatively similar sequence of transitions to those described above as the parameter driving the secondary flow (the coefficient of mass flow rate) is increased. At low mass flow rates, a steady solution with Z_2-symmetry results and at a critical flow rate, there is a symmetry-breaking Hopf bifurcation to a time-dependent flow where the streamsurface that coincided with the symmetry plane prior to the transition flip-flops between being attracted to the top and bottom rotating endwall boundary layers. Further increases in mass flux lead to quasi-periodic behaviour, frequency locking,

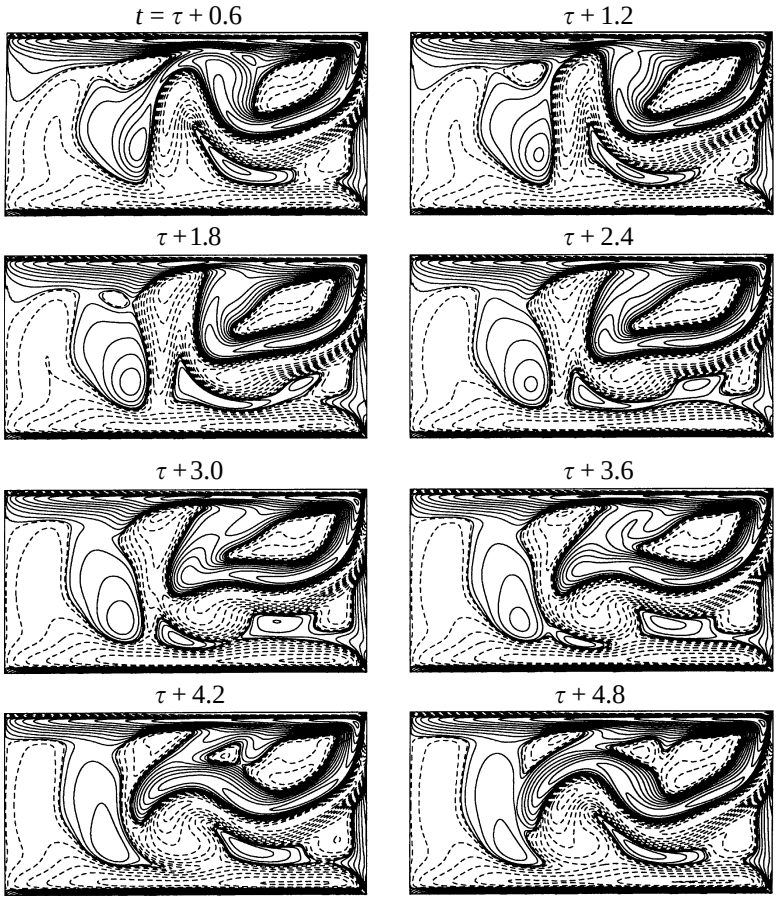

FIGURE 15. As figure 14 but for $s = -2.600$.

and eventually to chaotic behaviour. Although the details of the dynamics of the rotating annulus with a source/sink flow and those of the present differentially driven rotating cylinder flow are different, the two have qualitatively similar spatio-temporal behaviour.

7. Instability of the sidewall layer

In §4, we have seen that when the top is co-rotating with the cylinder, the flow is well described by similarity solutions of rotating disk flows, except in the vicinity of the sidewall, and that the radial extent for which this is true grows with Re. However, there is a limit to how large Re can go, as for sufficiently large Re the sidewall boundary layer becomes unstable. The stability of sidewall layers under these circumstances has only recently been investigated. Hart & Kittelman (1996) report some experimental observations of the sidewall instabilities and offer some tentative physical explanations for their origin, but conclude that their cause is not yet clear. The instabilities were observed to occur when the co-rotating top was rotating faster than the cylinder, i.e. $s > 1$, together with a fast basic rotation ($Re \sim O(10^5)$). Dijkstra & van Heijst (1983) also studied a similar differentially rotating system, but they only studied $s < 1$ and Re up to $\sim O(10^3)$; they did not report any instabilities of

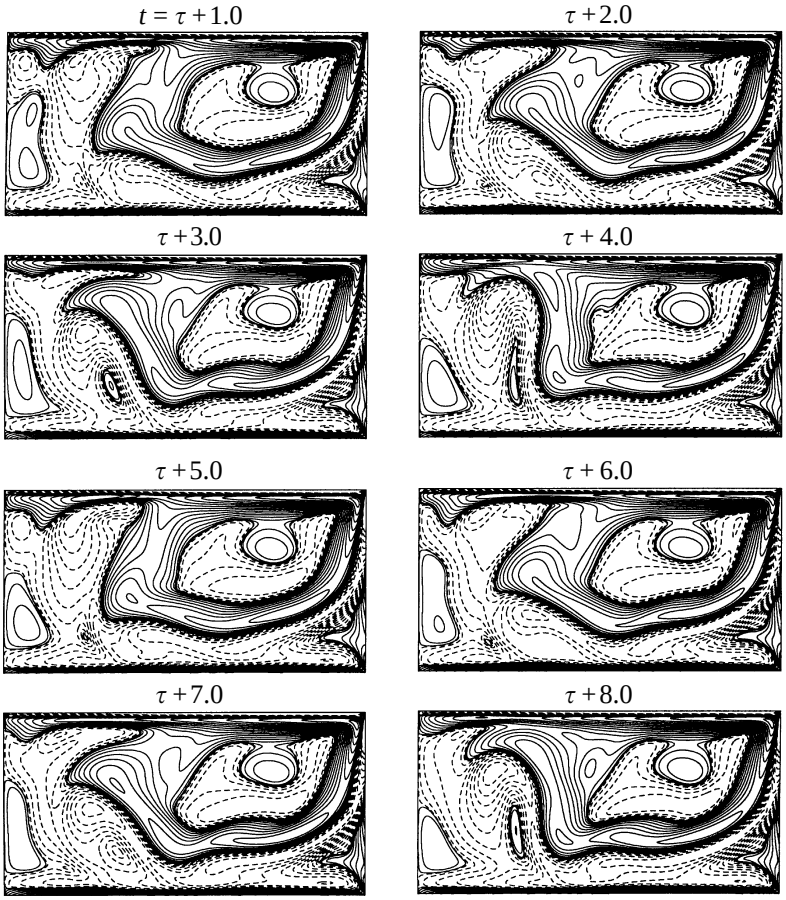

FIGURE 16. As figure 14 but for $s = -3.000$.

the sidewall. For $0 < s < 1$, we saw in §4 that the interior rotates as a solid body at a rate less than the sidewall, and that the difference in rotation rates is adjusted in a layer whose thickness depends primarily on Re and Λ, and to a much smaller degree on s. So, for $s < 1$, the sidewall boundary layer flow is centrifugally stable. Hart & Kittelman report that the instability first sets in as a series of axisymmetric rolls that propagate down the sidewall. They note that this first instability, as well as subsequent modes that appear at higher criticality, are qualitatively different to the sidewall instabilities in rotating channel flows and small-gap Taylor–Couette flows. They infer that the axisymmetric downward-traveling roll instability results from the centrifugal instability of the sidewall when $s > 1$; however they also note that the sidewall layer region also possesses a strong secondary meridional circulation driven by the differential rotation of the top.

Figure 19 gives radial profiles at $z = 0.5\Lambda$ of the azimuthal and axial components of vorticity, η and $\zeta = (1/r)\,\partial\Gamma/\partial r$, and of the axial and azimuthal components of velocity, w and v, for $Re = 6 \times 10^4$, $\Lambda = 0.5$ and $0.6 \leqslant s \leqslant 1.5$. The cases $s = 1.35$ and 1.5 are time periodic, and the profiles for these in the figure are at a particular time; the other cases are steady. This figure leads to a number of observations. All significant changes in the vorticity of the system occur in the boundary layers (unlike

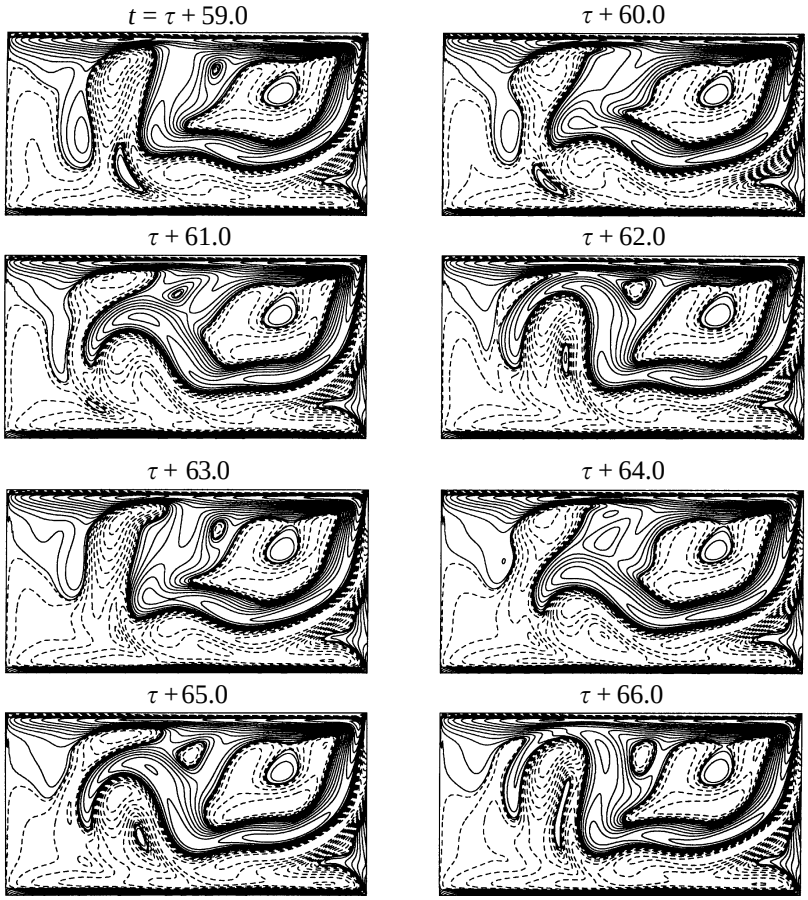

FIGURE 17. As figure 14 but for $s = -3.000$.

the situation when $s < 0$ where boundary layer separation leads to the formation of shear and transition layers in the interior). The structure of the sidewall layer is qualitatively different depending on whether $s > 1$ or $s < 1$. For $s = 1$, there is no sidewall layer as the fluid as a whole rotates with the cylinder and has constant vorticity directed parallel to the rotation axis of non-dimensional magnitude 2. As s increases (decreases) from 1, $(\zeta - 2)$ in the interior becomes positive (negative) and essentially independent of r, except near the sidewall, where at a location that depends weakly on s it changes sign. It is within this sidewall boundary layer region that the axial velocity w differs in any significant way from zero (it is non-zero in the interior, but there the axial velocity is very slow and directed from the slow to the fast disk). For $s < 1$, w becomes positive and finally zero on the sidewall without a change in the sign of curvature of its radial profile, whereas for $s > 1$, the radial profile of w is oscillatory as it approaches the sidewall, with $w \leqslant 0$ closest to the wall. Although w, the induced secondary flow component, is considerably smaller than v, the primary flow component, it can be expected to play a significant role in the dynamics of the sidewall layer: its radial gradient makes up the overwhelming majority of the azimuthal component of vorticity η. From figure 19, it is clear that η and ζ attain their maximum values on the sidewall, that their magnitudes are comparable there,

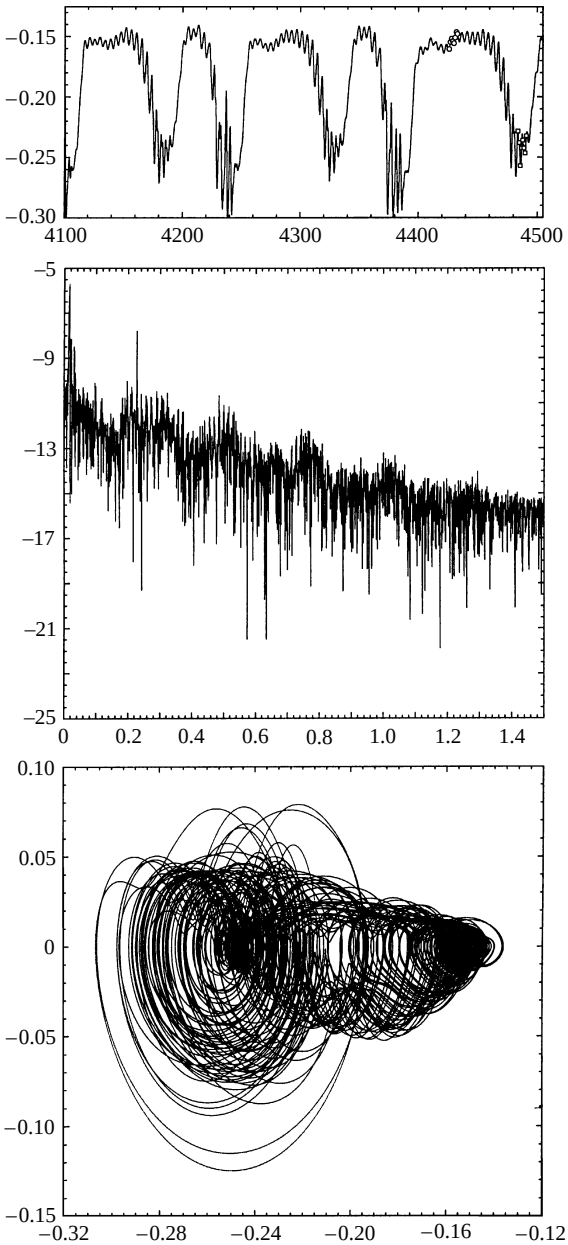

FIGURE 18. Detail of time series, PSD, and phase portrait of v_{mid} for $Re = 3 \times 10^3$, $\Lambda = 0.5$, and $s = -3.00$. Open circles and squares in the time series correspond to the snap-shots in figures 16 and 17 respectively.

but the radial gradients in η are much greater than those of ζ. This together with the fact that the radial profile of η for $s > 1$ is inflectional suggests that the sidewall boundary layer may become unstable due to the secondary flow rather than due to the centrifugal instability of the primary flow.

The above discussion is centred on the radial profiles at the cylinder half-height. Although the flow in the sidewall boundary layer is not parallel, i.e. it varies with

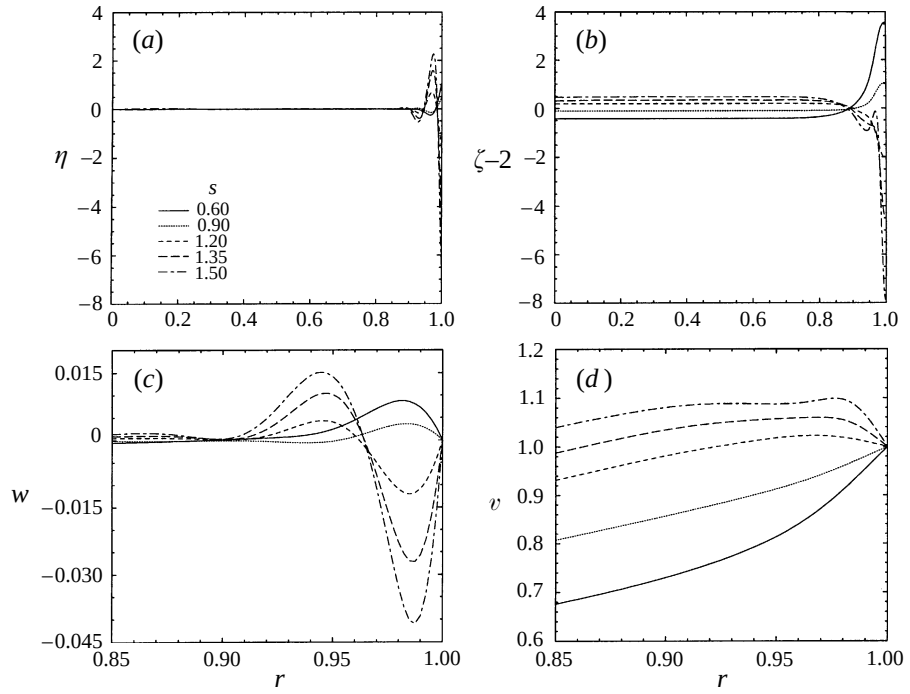

FIGURE 19. Radial profiles near the sidewall of (*a*) η, (*b*) $\zeta - 2$, (*c*) w and (*d*) v for $Re = 6 \times 10^4$, $\Lambda = 0.5$, and s as indicated.

z, this variation is not large, as is seen from the contours of η and ζ in figures 20 and 21. These figures show snap-shots over one period (≈ 2.4) of η and ζ in the region $0.8 \leqslant r \leqslant 1$, $0 \leqslant z \leqslant \Lambda$, for $Re = 6 \times 10^4$ and $s = 1.50$. These correspond approximately to the parameter values where Hart & Kittelman (1996) first observe the axisymmetric roll mode. There appears to be some difference between their roll instability and the axisymmetric waves in figures 20 and 21. Hart & Kittelman remark that the rolls are observed to originate near the corner where the top meets the sidewall and propagate down, whereas the waves in the figures originate much further down the sidewall. They propagate in the downwards direction for the waves closest to the wall, and they appear to be travelling along the path where w has a local extremum (in this case directed downwards). The wave disturbance is seen to turn around when it reaches the bottom and propagate upwards on the next extremum of w in from the sidewall. Note that since u is so small, the extrema in w correspond to the inflection points in η.

Related waves in boundary layer flows with a significant cross-flow component have also been observed by Savaş (1983, 1987), Lopez & Weidman (1996), Lopez (1996), Schouveiler *et al.* (1996), and Schouveiler, Le Gal & Chauve (1997). In those cases, the boundary layer in question is the endwall layer normal to the rotation axis, where the radial velocity u is the significant cross-flow component, w is negligible, and η in the boundary layer is essentially due to axial (z) gradients of u and has an oscillatory, i.e. inflectional, profile normal to the endwall. The waves were found to propagate along the inflection points in η in the local direction of the radial velocity (radially inwards). At sufficiently large Re, the second extremum in u in from the endwall, with u directed radially outwards, also carried waves radially outwards. In

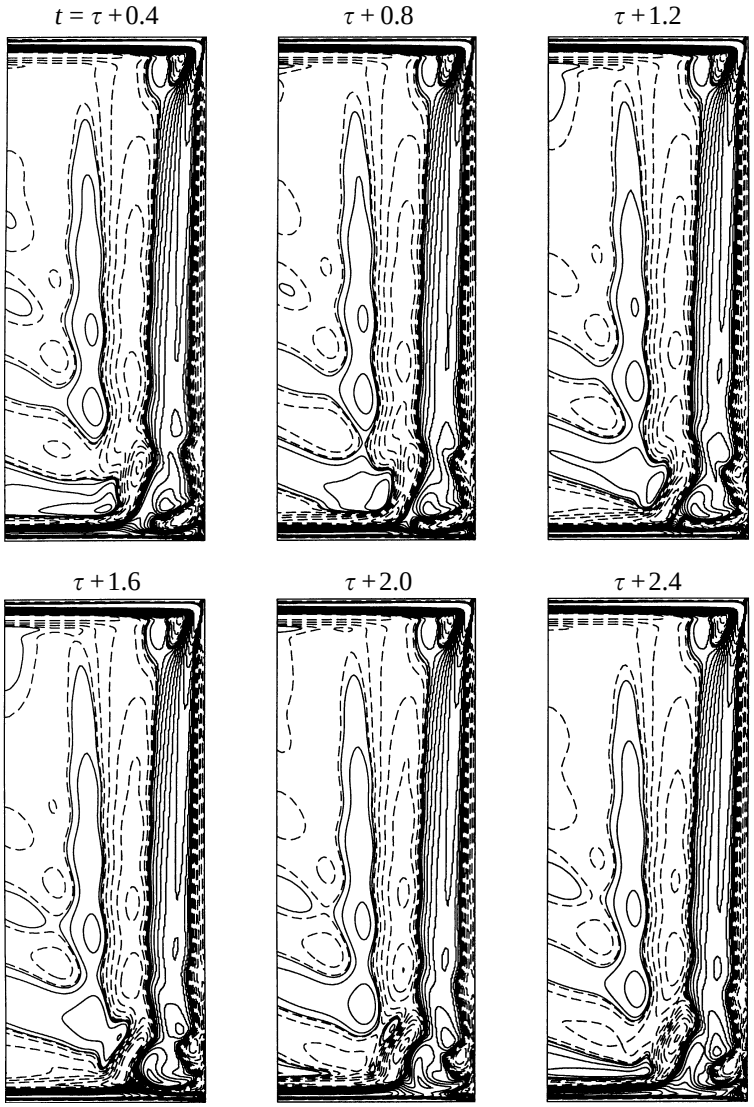

FIGURE 20. Contours of η near the sidewall ($0.8 \leqslant r \leqslant 1.0$) for $A = 0.5$, $Re = 6 \times 10^4$, and $s = 1.50$. Contour levels are set so that $\text{level}_i = \pm 10(i/15)^3$, $i = 1 \rightarrow 15$; positive (negative) contours are solid (broken).

both the endwall and the sidewall boundary layers, the observed (numerically and experimentally) axisymmetric waves appear to be due to an inflectional instability of the secondary flow (η). The experimental observations (Savaş 1983, 1987; Hart & Kettelman 1996; Lopez & Weidman 1996; Schouveiler *et al.* 1996, 1997) find in both cases that the first onset of instability is axisymmetric, and that as the effective Reynolds number in each case is increased, non-axisymmetric modes are excited. It is not yet clear whether the non-axisymmetric modes are due to a symmetry breaking of the axisymmetric mode or if they are due to a different mechanism, as some observations in the endwall layers (Savaş 1987; Schouveiler *et al.* 1997) and in the sidewall layer (Hart & Kittelman 1996) report the co-existence of both axisymmetric and spiral modes.

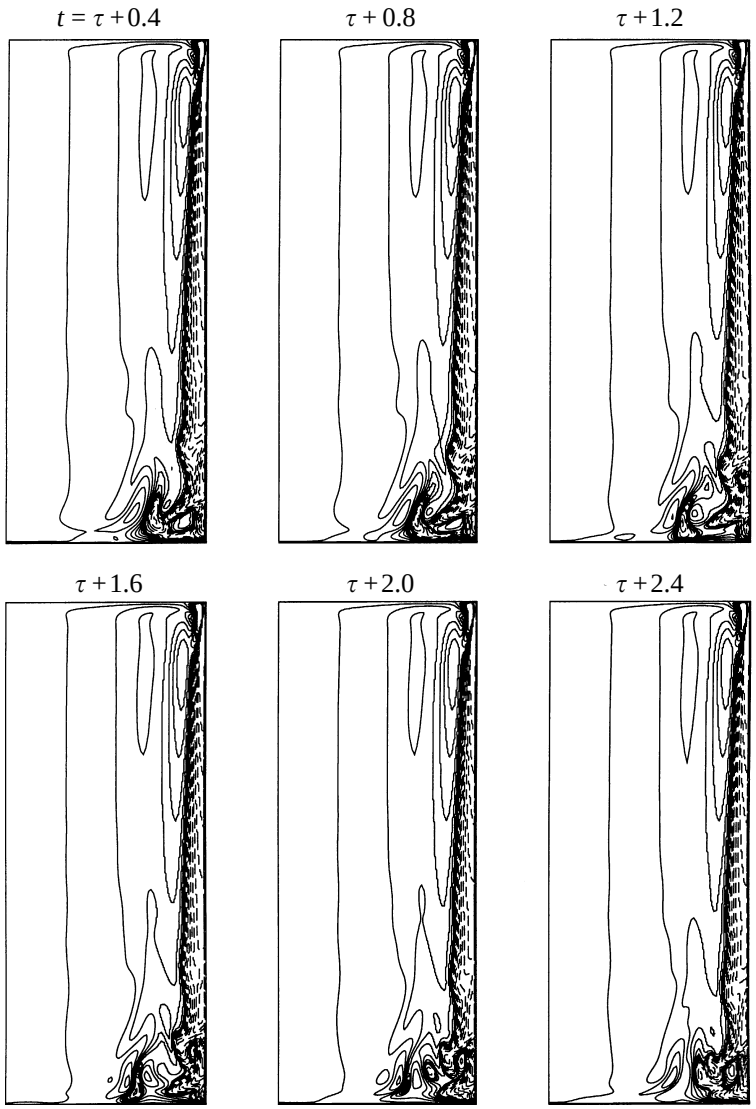

FIGURE 21. Contours of ζ near the sidewall ($0.8 \leqslant r \leqslant 1.0$) for $A = 0.5$, $Re = 6 \times 10^4$, and $s = 1.50$. Contour levels are set so that $\text{level}_i = \pm 10(i/15)^3$, $i = 1 \rightarrow 15$; positive (negative) contours are solid (broken).

8. Summary

A systematic study of the flow produced in a filled rotating cylinder by the differential rotation of its top endwall is presented. Qualitatively different phenomena are found as the differential rotation, measured by s, the ratio of the rotation rate of the top to that of the cylinder, is varied. For $s = 1$ the system is in solid-body rotation and for small deviations from $s = 1$, the bulk of the interior flow between the top and the bottom disk's boundary layers and away from the sidewall boundary layer is well described by matching similarity solutions of single disks of infinite radius rotating at the appropriate rates. This is so when the two disks are sufficiently apart so that there are distinct boundary layers associated with each, and the sidewall layer

is stable. When the top is co-rotating faster than the cylinder, i.e. $s > 1$, the sidewall layer is centrifugally unstable and the radial profile of the azimuthal vorticity near the sidewall is inflectional. At sufficiently large basic rotation rates of the cylinder, this situation leads to an instability of the sidewall that first manifests itself as a series of roll waves propagating down the sidewall layer.

With the top disk counter-rotating, its boundary layer separates to form a free shear layer. This shear layer is not simple; it consists of two parts, an azimuthal transition layer designated by the surface with $\Gamma = 0$ where the fluid rotates in opposite directions either side of it, and a meridional shear layer designated by the surface $\psi = 0$ where the fluid has a jet-like velocity profile along it. For sufficiently large Re, the two layers coincide outside the endwall and sidewall boundary layer regions and away from the immediate vicinity of the axis, i.e. away from regions where viscous stresses are important, when the flow is steady. When the flow is unsteady, they do not coincide in the interior either. The two layers will be susceptible to different types of instabilities. The meridional shear layer can be expected to be unstable primarily to axisymmetric disturbances, and these have been identified here resulting from a Hopf bifurcation. The azimuthal transition layer however, is most likely to be unstable to azimuthal disturbances. These are beyond the scope of the present investigation and are the subject of further study. Open questions remain as to whether the layer becomes unstable first via an axisymmetric Hopf bifurcation or via an azimuthal symmetry-breaking bifurcation as Re, s, and Λ are varied and what are the dynamics when the two bifurcations coincide resulting in high co-dimension bifurcations.

Much appreciation is given to Professor John Hart for the many discussions and the sharing of his experimental investigations of these flows, and to Professor Jie Shen for his invaluable help with the numerics. This work was partly supported by NSF grant DMS-9512483 and some of the computations were performed at the NCSA.

REFERENCES

Batchelor, G. K. 1951 Note on a class of solutions of the Navier–Stokes equations representing steady rotationally-symmetric flow. *Q. J. Mech. Appl. Maths* **4**, 29–41.

Beran, P. S. & Culik, F. E. C. 1992 The role of non-uniqueness in the development of vortex breakdown in tubes. *J. Fluid Mech.* **242**, 491–527.

Bödewadt, U. T. 1940 Die Drehströmung über festem Grunde. *Z. Angew. Math. Mech.* **20**, 241–245.

Brady, J. F. & Durlofsky, L. 1987 On rotating disk flow. *J. Fluid Mech.* **175**, 363–394.

Crespo del Arco, E., Maubert, P., Randriamampianina, A. & Bontoux, P. 1996 Spatio-temporal behaviour in a rotating annulus with a source-sink flow. *J. Fluid Mech.* **328**, 271–296.

Davis, S. H. & Rosenblat, S. 1977 On bifurcating solutions at low frequency. *Stud. Appl. Maths* **57**, 59–76.

Dijkstra, D. & Heijst, G. J. F. van 1983 The flow between two finite rotating disks enclosed by a cylinder. *J. Fluid Mech.* **128**, 123–154.

Gollub, J. P. & Swinney, H. L. 1975 Onset of turbulence in a rotating fluid. *Phys. Rev. Lett.* **35**, 927–930.

Hart, J. E. & Kittelman, S. 1996 Instabilities of the sidewall boundary layer in a differentially driven rotating cylinder. *Phys. Fluids* **8**, 692–696.

Kármán, Th. von 1921 Über laminare und turbulente Reibung. *Z. Angew. Math. Mech.* **1**, 233–252.

Khalili, A. & Rath, H. J. 1994 Analytical solution for a steady flow of enclosed rotating disks. *Z. Angew. Math. Phys.* **45**, 670–680.

Lance, G. N. & Rogers, M. H. 1962 The axially symmetric flow of a viscous fluid between two infinite rotating disks. *Proc. R. Soc. Lond.* A **266**, 109–121.

Lopez, J. M. 1994 On the bifurcation structure of axisymmetric vortex breakdown in a constricted pipe. *Phys. Fluids* **6**, 3683–3693.

LOPEZ, J. M. 1996 Flow between a stationary and a rotating disk shrouded by a co-rotating cylinder. *Phys. Fluids* **8**, 2605–2613.

LOPEZ, J. M. & SHEN, J. 1998 An efficient spectral-projection method for the Navier–Stokes equations in cylindrical geometries I. Axisymmetric cases. *J. Comput. Phys.* (to appear).

LOPEZ, J. M. & WEIDMAN, P. D. 1996 Stability of stationary endwall boundary layers during spin-down. *J. Fluid Mech.* **326**, 373-398.

MAXWORTHY, T. 1964 The flow between a rotating disk and a co-axial, stationary disk. *Space Programs Summary 37-27*, Vol. 4, Sec. 327. Jet Propulsion Laboratory, Pasadena, CA.

MULLIN, T. 1993 *The Nature of Chaos*. Oxford University Press.

MUNDT, M. D., HART, J. E. & OHLSEN, D. R. 1995 Symmetry, sidewalls, and the transition to chaos in baroclinic systems. *J. Fluid Mech.* **300**, 311–338.

ROGERS, M. H. & LANCE, G. N. 1960 The rotationally symmetric flow of a viscous fluid in the presence of an infinite rotating disk. *J. Fluid Mech.* **7**, 617–631.

ROTT, N. & LEWELLEN, W. S. 1967 Boundary layers and their interactions in rotating flows. *Prog. Aeronaut. Sci.* **7**, 111–144.

SAVAŞ, Ö. 1983 Circular waves on a stationary disk in rotating flow. *Phys. Fluids* **26**, 3445–3448.

SAVAŞ, Ö. 1987 Stability of Bödewadt flow. *J. Fluid Mech.* **183**, 77–94.

SCHOUVEILER, L., LE GAL, P. & CHAUVE, M. P. 1997 Spiral and circular waves in the flow between a rotating and a stationary disk. *Exps. Fluids* (submitted).

SCHOUVEILER, L., LE GAL, P., CHAUVE, M. P. & TAKEDA, Y. 1996 Experimental study of the stability of the flow between a rotating and a stationary disk. In *Advances in Turbulence VI* (ed. S. Gavrilakis *et al.*), pp. 385–388. Kluwer.

SHEN, J. 1997 Efficient spectral-Galerkin methods III. Polar and cylindrical geometries. *SIAM J. Sci. Comput.* **18**, 1583–1604.

ŠIL'NIKOV, L. P. 1965 A case of the existence of a denumerable set of periodic motions. *Sov. Math. Dokl.* **6**, 163–166.

STEWARTSON, K. 1953 On the flow between two rotating coaxial disks. *Proc. Camb. Phil. Soc.* **49**, 333–341.

ZANDBERGEN, P. J. & DIJKSTRA, D. 1977 Non-unique solutions of the Navier–Stokes equations for the Karman swirling flow. *J. Engng Maths* **11**, 167–188.